Resolving discharge parameters from atomic oxygen emission

P. Viegas[1]‡, L. Vialetto[1], A. W. van de Steeg[1], A. J. Wolf[1], W. A. Bongers[1], G. J. van Rooij[1,2,3], M. C. M van de Sanden[1,2], P. Diomede[1,3] and F. J. J. Peeters[1]

[1] DIFFER - Dutch Institute for Fundamental Energy Research, 5612 AJ Eindhoven, The Netherlands
[2] Department of Applied Physics, Eindhoven University of Technology, P. O. Box 513, 5600 MB Eindhoven, The Netherlands
[3] Faculty of Science and Engineering, Maastricht University, Zwingelput 4, ZW4, 6211 KH Maastricht, The Netherlands

E-mail: `viegas@mail.muni.cz`

6 May 2021

Abstract. A method is proposed to spatially resolve discharge parameters from experimental measurements of emission intensity and 1D numerical simulations including an O atom collisional-radiative model. The method can be used for different plasmas and conditions. Here, contracted microwave discharges for CO_2 conversion are studied at intermediate to high pressures (100 to 300 mbar). Radial profiles of electron density (n_e) are used as input in the model and corrected to successfully simulate the measured Gaussian profiles of emission intensity of the 777 nm transition (I_{777}). As a result, radially-resolved parameters inaccessible in experiments, such as n_e, power density (P_{abs}), electron temperature (T_e), electric field and reaction rates, are numerically-obtained for several conditions. n_e and P_{abs} approximately follow Gaussian profiles that are broader than that of I_{777}. For pressures below 150 mbar, the difference in full width at half maximum (FWHM) is typically a factor 1.6. This consists in a phenomenon of optical contraction, which is due to concave profiles of O molar fraction and T_e. The implications of the simulated profiles on the study of plasmas for CO_2 conversion are discussed and it is shown that these profiles allow to explain high reactor performances at low pressures.

‡ Present address: Department of Physical Electronics at the Faculty of Science, Masaryk University, Kotlářská 267/2, 611 37 Brno, Czech Republic

Resolving discharge parameters from atomic oxygen emission   2

1. Introduction

The understanding of low-temperature plasma physics and the optimisation of its applications is dependent on our knowledge of the spatial distributions of physical parameters in discharge reactors. Among those parameters, electron density (n_e), electron temperature (T_e), gas composition, gas temperature (T_g), reduced electric field (E/n_g), emission intensity and power density (P_{abs}) are often some of the most important. In fact, the spatial distribution of discharge parameters has been vastly studied but is only well established for specific discharge configurations. A well known example is the case in low pressure discharge regimes controlled by free diffusion or by ambipolar diffusion, where the radial distribution of n_e in a long cylindrical discharge follows a paraboloidal or a zero-order Bessel function of the first kind with zero at the cylinder wall [*Schottky*, 1924; *Parker*, 1963; *Ikegami*, 1968; *Durandet et al.*, 1989; *Lieberman and Lichtenberg*, 2005; *Fridman and Kennedy*, 2004; *Moisan and Pelletier*, 2012]. However, charged-particle balance in intermediate (a few to hundreds of mbar) to high pressure discharges relies on molecular ion recombination, and thus the Bessel profile cannot be assumed for cylindrical discharges in those conditions.

In several numerical and experimental works on glow and microwave (MW) discharges with atomic and molecular gases, n_e and emission intensity have been shown to have Bessel radial profiles at low pressures and currents when the discharge is diffuse, but significantly different, seemingly Gaussian profiles, at higher pressures or currents when the discharge contracts [*Petrov and Ferreira*, 1999; *Martinez et al.*, 2004; *Kabouzi et al.*, 2007; *Dyatko et al.*, 2008; *Golubovskii et al.*, 2011; *Shneider et al.*, 2014; *Golubovskii et al.*, 2017; *Ridenti et al.*, 2018; *Zhong et al.*, 2019]. In particular, in the work of *Dyatko et al.* [2008] with a 1D-radial model describing an argon glow discharge at intermediate pressure, the ratio between the peak and the average electron densities has been calculated to change from 2.3 for a Bessel profile to 720 for a highly contracted discharge. Then, in *Carbone et al.* [2012], radially-resolved n_e measurements through Thomson scattering in a MW argon plasma at intermediate pressure have been fitted with a Bessel function for which the boundary radius R defined by $n_e(R) = 0$ is a free parameter that decreases with pressure. Furthermore, in the 1D models in *Gregório et al.* [2010, 2012] of argon MW microplasmas at atmospheric pressure, n_e contracts to a concave shape that is neither Gaussian nor Bessel. On the contrary, in the 2D numerical work in *Baeva et al.* [2018] in an argon plasma torch at atmospheric pressure, the radial profile of n_e presented is rather flat.

Radiative emission takes place naturally in reactive plasmas, and therefore emission intensity can be an easily accessible source of spatially-resolved information in the discharge. Nevertheless, in contracted conditions, the n_e profile can be spatially more extended than the optical appearance of the plasma suggests. Indeed, experimental radial distributions of line emission have been reported to be more compressed than that of n_e (obtained from the Bremsstrahlung continuum) in neon in *Golubovskii et al.* [2011] and in helium in *Golubovskii et al.* [2020]. This effect has been called optical contraction

and has been attributed in *Golubovskii et al.* [2011] to the influence of electron-electron collisions on the electron energy distribution function (EEDF), which enhances electron-impact excitation and ionisation reactions in the centre of the discharge. However, in *Golubovskii et al.* [2020], this effect seems to be due to the low values of E/n_{g} in the radial edges, as E/n_{g} is theoretically estimated to have a significantly concave distribution in that work. The concave shape of E/n_{g} is in agreement with the experimental measurements and simulations of concave profiles of T_{e} in *Kabouzi et al.* [2007]; *Gregório et al.* [2010]; *Golubovskii et al.* [2011]; *Gregório et al.* [2012]; *Golubovskii et al.* [2017]; *Ridenti et al.* [2018]; *Zhong et al.* [2019]. In fact, the simulations in *Ridenti et al.* [2018] have shown that T_{e} in Thomson scattering measurements, such as those in *van Gessel et al.* [2012]; *Carbone et al.* [2012], has a convex radial profile due to the Maxwellian assumption of this diagnostic, while T_{e} obtained from the calculated EEDF (2/3 of mean electron energy) actually has a concave radial profile, as does E/n_{g}. Conversely, the T_{e} and E/n_{g} radial profiles obtained in the 1D and 2D simulations in *Martinez et al.* [2004]; *Jimenez-Diaz et al.* [2012]; *Georgieva et al.* [2017]; *Baeva et al.* [2018] have been reported as approximately radially homogeneous. We can conclude that the relationships between the spatial profiles of different discharge parameters so far are not completely understood and cannot be generalised.

In this work, we address the spatial distribution of discharge parameters in MW CO_2 plasma reactors. These are intended to convert greenhouse gas CO_2 into carbon-neutral fuels or useful chemicals [*Goede et al.*, 2014; *Guerra et al.*, 2017; *Snoeckx and Bogaerts*, 2017; *Vermeiren and Bogaerts*, 2020]. Spatial distributions in these discharges are particularly interesting, as the discharge radius has been shown to have a strong correlation with reactor performance, with the best conversion and energy efficiencies having been obtained when the core of the discharge has a radially-contracted structure [*Fridman*, 2008; *van Rooij et al.*, 2015; *den Harder et al.*, 2017; *Bongers et al.*, 2017]. In particular, the relationship between the spatial distribution of P_{abs} and the reactor performance has been highlighted in *van den Bekerom et al.* [2019].

Recent studies have addressed the contraction dynamics and the radial structure of MW discharges for CO_2 conversion [*Wolf et al.*, 2019; *Groen et al.*, 2019; *Wolf et al.*, 2020b, a; *Viegas et al.*, 2020; *D'Isa et al.*, 2020]. The contraction of a vortex-stabilised CO_2 MW plasma has been characterised in *Wolf et al.* [2019] in relation to its dielectric properties. Then, in *Wolf et al.* [2020b], two distinct contracted discharge modes have been identified and described at pressures above 85 mbar: a low-confinement L-mode at lower pressures and at temperatures between 3000 and 5000 K and a high-confinement H-mode at higher pressures and at temperatures above 5500 K. The works in *Viegas et al.* [2020] and *Wolf et al.* [2020a] have investigated the contracted modes numerically. The distinct changes in spatial profiles of n_{e} and P_{abs} with discharge modes have been shown to be important to obtain accurate descriptions of the reactivity within the plasma, that determines the spatial structure of the plasma itself [*Viegas et al.*, 2020], as well as of the follow-up reactions of plasma products in its periphery, that influence the reactor performance [*Wolf et al.*, 2020a]. Despite the importance of accurately determining

these spatial profiles, discharge parameters are difficult to measure with mm resolution in CO_2 MW plasmas and are often based on the spatial distribution of parameters that are easier to obtain experimentally, such as the radiative emission intensity. As such, the works on CO_2 discharge contraction so far have relied on unverified simplifying assumptions on the spatial profiles of discharge parameters, such as n_e, P_{abs} and E/n_g. To self-consistently describe the relationships between these parameters and improve profile determination, it is very relevant to assess the assumptions used so far.

In this work, numerical simulations are used to determine spatially-resolved discharge parameters in a CO_2 MW discharge from the experimentally measured intensity distribution of the 777 nm spectral line emission of atomic oxygen: $O(3p$ $^5P) \rightarrow O(3s\ ^5S^0)$ (I_{777}). This study requires a collisional-radiative model (CRM) of O atom kinetics. That type of description has been developed and used in works such as *Dagdigian et al.* [1988]; *Stancu et al.* [2016]; *Caplinger and Perram* [2020]; *Fiebrandt et al.* [2020]. In particular, in *Fiebrandt et al.* [2020] a CRM has been developed to calculate excited state densities of atomic oxygen in zero dimensions in low pressure plasmas with varying Ar/O_2 mixtures. That work has highlighted the influence of radiative cascading between excited states and of radiation self-absorption. Moreover, in *Caplinger and Perram* [2020] a CRM focused on the 777 nm/844 nm line ratio of atomic oxygen has been developed in zero dimensions to study oxygen plasmas at different pressures and with different dissociation degrees (ratio between O and O_2). The results of that CRM have been compared with those of more commonly-used models, such as the extended corona model. The relevance of stepwise excitation and cascade emission has been put forward in *Caplinger and Perram* [2020]. Both of these recent works have discussed the choice and use of kinetic data in their CRMs.

This paper employs for the first time a CRM for atomic oxygen developed in the context of reactive CO_2 mixtures at intermediate to high pressures (100 to 300 mbar). We use it in 1D to radially resolve n_e, T_e, E/n_g and P_{abs} in contracted MW discharges for CO_2 conversion. In section 2, the experimental set-up is presented, along with the plasma conditions and the measurements undertaken. The set of hypotheses taken in the interpretation of experiments to relate the experimentally-measured Gaussian profiles $I_{777}(r)$ to the other discharge parameters is also explained. Then, the 1D-radial model developed in this work is explained in section 3, including the CRM for atomic oxygen. The simulation results are presented in section 4 for the different sets of conditions presented in section 2. First, an $n_e(r)$ profile calculated directly from experimental data is used as input in the simulations, in order to illustrate the shortcomings of some of the hypotheses taken. The dependence of $n_e(r)$ on $I_{777}(r)$, and vice-versa, is obtained and explained from the simulations, and leads to correcting the hypotheses considered so far and the assumptions for $n_e(r)$. The simulations show that the corrected assumptions are consistent with the measurements, and thus provide radially-resolved discharge parameters. Finally, the implications of these findings on the study of MW discharges for CO_2 conversion are demonstrated and discussed, along with the possibilities to apply this correction procedure to relate discharge parameters in different plasmas.

Resolving discharge parameters from atomic oxygen emission   5

2. Experimental set-up, hypotheses and conditions

2.1. Experimental set-up and hypotheses on plasma parameters

The discharges studied in this work are obtained experimentally in a vortex-stabilised microwave reactor. This configuration has been used in several works on plasma-driven CO_2 conversion [*Butylkin et al.*, 1981; *Fridman*, 2008; *Bongers et al.*, 2017]. The set-up is presented in figure 1 and described in more detail in *Wolf et al.* [2019]. It consists of a 2.45 GHz microwave source, a rectangular waveguide field applicator and a 3-stub tuner for impedance matching. The electromagnetic (EM) field is continuously coupled to a CO_2 gas flow, which is contained in a quartz tube of inner radius $R_{\text{tube}} = 13.5$ mm. The wave electric field is directed parallel to the discharge tube (transverse-electric (TE_{10}) single mode standing wave). The plasma is stabilised in the center of the tube by means of a vortex flow, achieved by tangential gas injection, to prevent plasma-induced wall damage, as in *Fleisch et al.* [2007]. The discharge characteristics and the related performance of CO_2 conversion to CO in this reactor have been studied in detail in recent years in *Wolf et al.* [2019, 2020b]; *Pietanza et al.* [2020]; *Wolf et al.* [2020a]; *Viegas et al.* [2020].
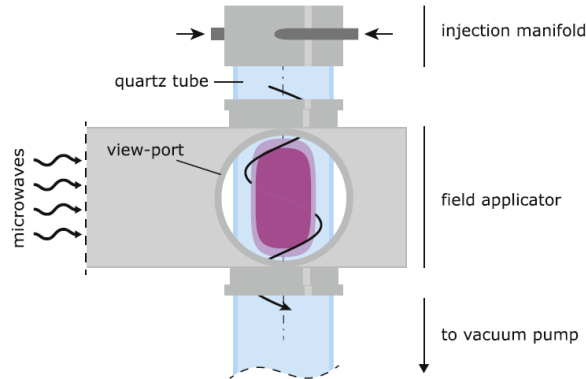
Figure 1. Illustration of the experimental setup, including the main plasma reactor components. Figure from *Wolf et al.* [2020b].

In *Wolf et al.* [2019], the intensity distribution of the 777 nm spectral line emission of atomic oxygen (O(3p ^{5}P) $\rightarrow$ O(3s ^{5}S^0)) has been measured to have a Gaussian radial profile $I_{777}(r)$ with full width at half maximum (FWHM) Λ_{777} and characteristic width (or standard deviation) $\sigma_{777} = \Lambda_{777}/\left(2\sqrt{2\ln(2)}\right)$, that are invariant under an Abel transform:

$$I_{777}(r) = I_{777}(0)\exp\left(-\frac{1}{2}\frac{r^2}{\sigma_{777}^2}\right) \tag{1}$$

It is assumed in *Wolf et al.* [2019] that $n_{\text{e}}(r)$ also follows a Gaussian radial profile, with peak $n_{\text{e}0}$, and is proportional to $I_{777}(r)$, with a proportionality parameter s, such that:

$$n_{\text{e}}(r) = n_{\text{e}0}\exp\left(-\frac{1}{2}\frac{r^2}{(\sqrt{s}\sigma_{777})^2}\right), 1 \leq s \leq 2 \tag{2}$$

That assumption is based on the following hypotheses:

1) The upper state of the 777 nm emission, $O(3p\ ^5P)$, of density $n_{O(3p\ ^5P)}$, is produced mostly by electron-impact excitation of the atomic oxygen ground-state $O(2p^4\ ^3P)$, of density $n_{O(2p^4\ ^3P)}$, with rate coefficient $k_{exc}(T_e)$. $O(3p\ ^5P)$ is mostly destroyed by radiative emission with coefficient τ_{rad}^{-1} and quenching by any neutral species (with gas density n_g) with coefficient k_Q. The radiation balance is then expressed as:

$$I_{777} = \tau_{rad}^{-1} n_{O(3p\ ^5P)} \simeq \tau_{rad}^{-1} \frac{n_e\ n_{O(2p^4\ ^3P)}\ k_{exc}(T_e)}{\tau_{rad}^{-1} + n_g\ k_Q} \tag{3}$$

2) τ_{rad}^{-1} and k_Q are radially homogeneous, and $n_g k_Q > \tau_{rad}^{-1}$. Thus:

$$I_{777} \propto n_e\ x_O\ k_{exc}(T_e), \tag{4}$$

where $x_O = n_{O(2p^4\ ^3P)}/n_g$.

3) E/n_g and T_e are radially homogeneous in the plasma region, and so is $k_{exc}(T_e)$.

4) x_O is defined by heavy-particle thermal reactions that are independent of n_e, and by electron-impact reactions with rates proportional to n_e. It is assumed that:

$$I_{777} \propto n_e^s, 1 \leq s \leq 2 \tag{5}$$

The line-integrated electron density at the axial centre of the discharge ($n_{e\Lambda}$) has been measured in *Wolf et al.* [2019], and thus the peak of n_e and the plasma diameter Λ_{n_e} (FWHM of the $n_e(r)$ profile) have been calculated according to the assumption in eq. 2 as function of s:

$$n_{e0} = n_{e\Lambda}/\sqrt{2\pi(\sqrt{s}\sigma_{777})^2} \tag{6}$$

$$\Lambda_{n_e} = \sqrt{s}\Lambda_{777} \tag{7}$$

Using these hypotheses, in *Wolf et al.* [2019] the radius of the discharge column and the skin-depth of wave absorption have been found to have approximately the same value, for $1 \leq s \leq 2$. Then, in the subsequent studies of this discharge [*Groen et al.*, 2019; *Wolf et al.*, 2020b; *Pietanza et al.*, 2020; *Wolf et al.*, 2020a; *Viegas et al.*, 2020], as well as in the investigation of a similar CO_2 MW discharge [*D'Isa et al.*, 2020], the assumption in eq. 2 has been used, with additional hypotheses:

5) x_O is defined by thermal chemistry and the radial gradient of gas temperature is lower than the one of n_e. Hence, x_O is radially homogeneous in the plasma region, and therefore:

$$s = 1; n_e(r) = n_{e0}\ \exp\left(-\frac{1}{2}\frac{r^2}{\sigma_{777}^2}\right) \tag{8}$$

6) As the temperature, composition, E/n_g, T_e and electron collision frequency ν_c are considered radially homogeneous, the microwave absorbed power density (P_{abs}) is assumed to have the same radial profile as n_e [*Wolf et al.*, 2020b]:

$$P_{abs}(r) = P_{abs0}\ \exp\left(-\frac{1}{2}\frac{r^2}{\sigma_{777}^2}\right), \tag{9}$$

where P_{abs0} is obtained by dividing the total input power by the normalised volume integral of the emission intensity.

Resolving discharge parameters from atomic oxygen emission 7
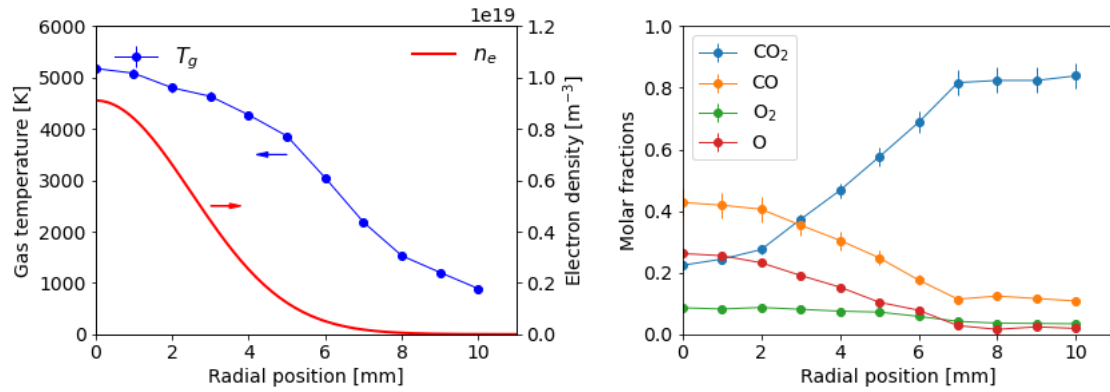
2.2. Experimental conditions

In this paper, we use the model described in section 3 to evaluate the hypotheses listed in section 2.1 and to spatially resolve discharge parameters. Here we describe the different sets of experimental conditions considered as input in the model.

2.2.1. Condition A: low-confinement discharge

Firstly, a discharge in low-confinement mode, according to the definition in *Wolf et al.* [2020b], is studied. This is a well characterised discharge, which is contracted but with Λ_{777} close to half the tube diameter. It has been obtained at 110 mbar with a fixed steady-state input power of 950 W and a flow rate of 9 slm. The Gaussian-shaped emission intensity of the 777 nm line (following eq. 1) has a radial FWHM $\Lambda_{777} = 5.88$ mm and an axial FWHM $L_{777} = 21.40$ mm. The line-integrated electron density $n_{e\Lambda}$ has been measured through 140 GHz microwave interferometry and the profile $n_e(r)$ has been assumed according to eqs. 6-8. The relative uncertainty in the measurement of $n_{e\Lambda}$ is of the order of 100% for pressures below 110 mbar and then decreases with pressure, reaching values of the order of 10% for pressures above 200 mbar [*Wolf et al.*, 2019; *Viegas et al.*, 2020]. This diagnostic considers the plasma as an infinite homogeneous slab, which applies when the plasma size is large compared to the diagnostic beam dimensions. Since this approximation collapses under the narrow plasma conditions considered in this work, a correction factor is applied which accounts for the partial pass-through of the diagnostic beam through the plasma medium. This correction has not been considered in previous works [*Wolf et al.*, 2019; *Groen et al.*, 2019; *Viegas et al.*, 2020], which might lead to an underestimation of n_e in those works. The partial pass-through effect is accounted for by applying a correction factor α, whose calculation is further described in *Mousavi et al.* [2021], such that:

$$n_{e\Lambda,\text{corrected}} = n_{e\Lambda,\text{measured}} \times \alpha \tag{10}$$

The correction factor α is inversely proportional to the interferometry frequency and to Λ_{777}. In the current case, $\alpha = 1.32$ and the corrected $n_{e0} = 9.11 \times 10^{18}$ m^{-3}. The rotational temperature (taken as the same as the translational temperature T_g) and the densities of the main species in the plasma reactor (CO_2, CO, O_2 and O) are measured locally at the axial position of the centre of the waveguide with 1 mm radial resolution through spontaneous rotational Raman scattering. This diagnostic has been used to measure temperature in *van den Bekerom et al.* [2019, 2020]; *van de Steeg et al.* [2020] and is further explained in *van de Steeg et al.* [2021]. As pointed out in our previous works assessing measurements and simulations of the main neutral species densities [*Wolf et al.*, 2020a; *Viegas et al.*, 2020; *van de Steeg et al.*, 2021], their value and spatial distribution are determined mostly by thermally-driven neutral chemistry and by fast transport processes. The data taken as input in the model are presented in figure 2. On the left side of the figure, the assumed profile $n_e(r)$ and the measured profile $T_g(r)$, and on the right side, the measured molar fractions of the main species.

Resolving discharge parameters from atomic oxygen emission   8

Figure 2. Radial profiles of experimental input parameters in condition A (950 W, 9 slm and 110 mbar). On the left, the assumed $n_e(r)$ and the measured $T_g(r)$. On the right, the measured molar fractions of CO_2, CO, O_2 and O.

2.2.2. Condition B: high-confinement discharge

The main characteristics of the studied discharges are defined by their confinement degree, which is largely dependent on input power and pressure [*Wolf et al.*, 2020b]. As such, it is important to evaluate discharge parameters also in high-confinement mode. A flow rate of 12 slm is used, and a high-confinement discharge is obtained at 150 mbar with an input microwave power of 860 W. T_g and composition are measured through Raman scattering, $n_{e\Lambda}$ is measured through 140 GHz interferometry and $n_e(r)$ is assumed through eq. 8 after considering the correction factor α, as for condition A. The length L_{777} is 26.71 mm, the diameter Λ_{777} is 2.46 mm, below half of that of condition A, and the correction factor α is 2.69. $n_e(r)$ and $T_g(r)$ are represented on the left side of figure 3. The measured composition is shown on the right side of the same figure. The $n_e(r)$ and $T_g(r)$ profiles clearly have sharper gradients than in condition A and, as a result of the higher temperature, the CO and O molar fractions are higher and have broader profiles than in condition A.
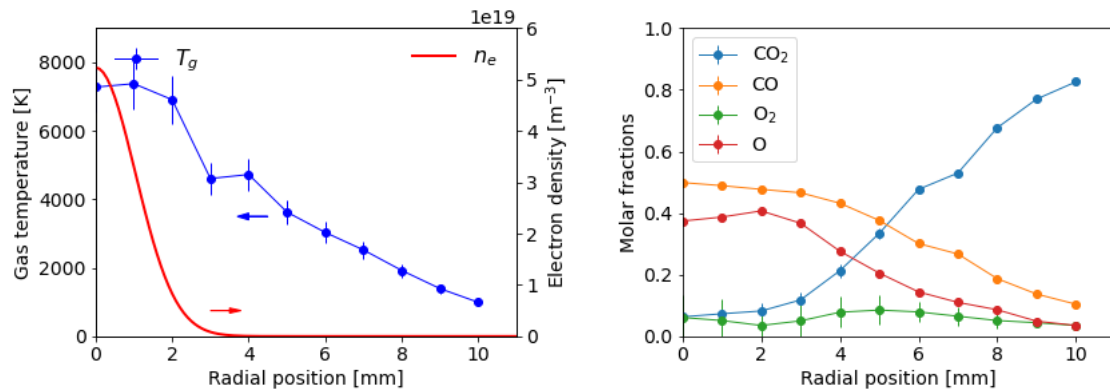
Figure 3. Radial profiles of experimental input parameters in condition B (860 W, 12 slm and 150 mbar). On the left, the assumed $n_e(r)$ and the measured $T_g(r)$. On the right, the measured molar fractions of CO_2, CO, O_2 and O.

Resolving discharge parameters from atomic oxygen emission 9

p [mbar]	L_{777} [mm]	Λ_{777} [mm]	α	n_{e0} [10^{18} m^{-3}]	$T_{g,max}$ [K]
108	12.1	6.44	1.09	1.61	4927
121	15.4	4.77	1.25	8.24	5562
141	18.9	3.97	1.40	24.62	6082
161	22.5	3.68	1.47	26.75	6220
209	34.4	3.64	1.48	53.58	6119
249	34.6	3.50	1.53	71.30	6064
296	57.5	3.56	1.51	98.45	6007

Table 1. Experimental input parameters in the set of conditions C: Pressure, length, diameter, n_e correction factor, corrected n_e peak and maximum of T_g.

2.2.3. Set of conditions C: input from flow modelling

In some high-confinement conditions, emission from C_2 is present in the plasma (although C_2 remains a minor constituent), which severely cripples the Raman scattering diagnostic. Therefore, it is relevant to study spatial profiles of discharge parameters in cases where neutral composition is known from simulation results, which also allows wider parameter scans. Unlike the case in conditions A and B, in the set of conditions C we take the radial distributions of T_g and neutral composition from the simulation results of the 2D model in *Wolf et al.* [2020a], at the axial position of maximum temperature. In that work, the peak gas temperature in the centre of the discharge has been taken as input from Doppler broadening measurements of the 777 nm atomic oxygen line emission [*Wolf et al.*, 2019]. We study 7 discharge conditions in different confinement modes by changing only pressure. They are obtained with 1400 W input power and 18 slm flow rate and the pressure is increased from 108 mbar to 296 mbar. These conditions are described in *Wolf et al.* [2019] and in *Viegas et al.* [2020]. However, the plasma dimensions considered here have been found as in *Wolf et al.* [2020a], in a slightly different way than in the previous works. $n_e(r)$ is obtained from eq. 8, with $n_{e\Lambda}$ measured from 168 GHz interferometry. Although n_{e0} is displayed in *Wolf et al.* [2019] and in *Viegas et al.* [2020], the correction factor α is not taken into account in the values in those works. For the sake of brevity, the radial profiles of n_e, T_g and composition are not represented here, but $T_g(r)$ and the molar fraction $x_O(r)$ are shown later in figure 13. Moreover, some of the main plasma parameters are listed in table 1. It can be noticed from Λ_{777} in table 1 that the confinement degree of these discharges (except at 108 mbar) stands between the ones of conditions A and B. Furthermore, that is also the case for $T_{g,max}$ and, as such, the degree and extension of dissociation in these plasmas are also in between those of condition A (figure 2) and those of condition B (figure 3).

Main neutral species	CO_2, CO, O_2, $O(2p^4\ ^3P)$, C
Charged species	e, O^-, CO_2^+, CO^+, O_2^+, O^+, C^+
Metastable states	$O(2p^4\ ^1D)$ [1.97 eV], $O(2p^4\ ^1S)$ [4.19 eV]
	$O(3s\ ^5S^0)$ [9.15 eV], $O(3s\ ^3S^0)$ [9.52 eV]
Radiative states	$O(3p\ ^5P)$ [10.74 eV], $O(3p\ ^3P)$ [10.99 eV]
	$O(3d\ ^5D^0)$ [12.08 eV], $O(3d\ ^3D^0)$ [12.09 eV]

Table 2. List of species considered in the model, along with the internal energies of O excited states [*Laher and Gilmore*, 1990; *Kramida et al.*, 2020].

3. Numerical model

3.1. 1D-radial plasma fluid model

Resolving discharge parameters in space requires at least a one-dimensional (1D) description of the CO_2 conversion MW plasma. In this work, we have developed and used an in-house 1D-radial fluid model addressing the plasma at the core axial position, *i.e.* the position of the centre of the waveguide. The species in table 2 are considered. The model consists in solving for every species k the steady-state mass balance equations of the form:

$$\nabla \cdot \mathbf{\Gamma}_k = \frac{1}{r}\frac{d}{dr}\left(-rD_k\frac{d}{dr}[y_k\rho]\right) + \left(\frac{\Gamma_{out,k}}{L} - \frac{\Gamma_{in,k}}{L}\right)_z = m_k\left(\sum_j S_{j,k} - \sum_i L_{i,k}\right) \quad (11)$$

where r is the radial coordinate, y_k is the mass fraction of species k and ρ is the total mass density of the mixture ($\rho = \sum_k m_k n_k = \sum_k y_k\rho$). $\mathbf{\Gamma}_k$, D_k, n_k and m_k are, respectively, the flux of mass density, the mass diffusion coefficient, the number density and the particle mass of species k. $S_{j,k}$ and $L_{i,k}$ are, respectively, the chemistry source and loss terms associated to reactions j and i acting on species k. The reactor under study is characterized by vortex-stabilization, a recirculation zone, turbulent transport and, therefore, complex flow patterns. As such, the local transport is largely unknown and in this model, motivated by the work in *Wolf et al.* [2020a], we describe it as being mostly determined by laminar and turbulent mass diffusion. The model therefore consists mostly of a reaction-diffusion description. An axial convective transport term is included as in *Wolf et al.* [2020a]; *Viegas et al.* [2020], in the form of $\left(\frac{\Gamma_{out,k}}{L} - \frac{\Gamma_{in,k}}{L}\right)_z$, where L is the plasma length taken from the emission intensity as $L = L_{777}$, $\Gamma_{in,k}$ is the flux of CO_2 entering the plasma length, and $\Gamma_{out,k}$ is the flux of every product exiting the plasma. These fluxes are calculated from the conservation of mass flow rate as:

$$\Gamma_{k,z}(r) = m_k n_k(r) v_z(r) \quad (12)$$

$$v_z(r) = \frac{\dot{m}}{\rho(r)A} \quad (13)$$

where $v_z(r)$ is the axial convective velocity at position r, $\dot{m}$ is the input mass flow rate of CO_2 at room-temperature and at reactor pressure and A is the tube cross section $A = \pi(13.5\ \text{mm})^2$.

As the electric field associated to the MW propagation in transverse-electric mode in the experiments is not axisymmetric, this model does not include the simulation of electric field through Maxwell's equations. Instead, an electron density profile $n_{e,IN}(r)$ (considering eq. 2 dependent on s) is assumed and E/n_g at each position r is self-consistently calculated by iterating this parameter until the electron density $n_e(r)$ matches $n_{e,IN}(r)$. $n_e(r)$ is obtained from the ion densities through a quasi-neutrality assumption. As such, only the electric field magnitude is considered, and not its direction, which leads us to neglecting electric drift and charge separation. The convergence criteria of the simulation are twofold. One criterion consists in matching $n_e(r)$ with $n_{e,IN}(r)$ within 1%, for every position where $n_{e,IN}(r) > 7 \times 10^{16}$ m^{-3}. We should notice that this tolerance is lower than the experimental uncertainty. For positions with lower electron density, $n_e(r)$ is not required to match $n_{e,IN}(r)$ and the reduced electric field E/n_g is assumed to be 1 Td, taken as a minimum value in the simulations. The other convergence criterion consists in imposing a solver tolerance for residuals of mass fractions of 10^{-6}. The model takes quantities from experiments presented in section 2 as input: p, L_{777}, flow rate, $n_{e,IN}(r)$ (where $n_{e\Lambda}$ and Λ_{777} are included), $T_g(r)$ and radially-resolved composition. Concerning $T_g(r)$ and composition, a linear interpolation is taken in between measured points. For $r > 10$ mm, where measurements are not available, the values at $r = 10$ mm are assumed. The influence of experimental uncertainties associated to quantities used as input in the model, such as n_e and T_g, in plasma chemistry simulation results has been put forward in *Viegas et al.* [2020]. As the electron density is obtained from quasi-neutrality, the simulations solve eq. 11 for a total of 15 species: C, O$^-$, CO$_2^+$, CO$^+$, O$_2^+$, O$^+$, C$^+$ and the metastable and radiative excited states of atomic oxygen. The mass fraction of ground-state O(2p^4 ^{3}P) is obtained from subtracting the mass fractions of the O excited states O(i) to the input one of O as $y_{O(2p^4\ ^3P)} = y_O - \sum_i y_{O(i)}$. The measured molar fractions of CO$_2$, CO, O$_2$ and O are given as input to the model and allow to calculate $\rho(r)$ according to the ideal gas law. Then, the mass fractions of these species are slightly adjusted during the simulations in order to preserve the ideal gas law. The reactions corresponding to the chemistry source terms $S_{k,j}$ are described in section 3.2.

As radial transport in the reactor under study is largely unknown, we describe it for the 15 species in the same way as in *Wolf et al.* [2020a], where simulation results have found good experimental agreement. Radial transport is described in this model through laminar and turbulent Fickian mass diffusion, with the diffusion coefficient of each species k defined as the sum of a laminar coefficient $D_{L,k}$ and an effective turbulent coefficient D_T:

$$D_k(r) = D_{L,k}(r) + D_T(r) \tag{14}$$

The turbulent diffusion coefficient is taken from *Wolf et al.* [2020a], where it is defined independently of the mixture as:

$$D_T(r) = \frac{\nu_T(r)}{Sc_T}, \tag{15}$$

Resolving discharge parameters from atomic oxygen emission   12

with constant turbulent Schmidt number $Sc_{\mathrm{T}} = 0.71$ [*Yimer et al.*, 2002], and turbulent viscosity $\nu_{\mathrm{T}}(r)$. The same formulation has been adopted in *Synek et al.* [2015]. In *Wolf et al.* [2020a], in agreement with Computational Fluid Dynamics simulations of the vortex flow including a plasma heat source, it is stated that the radial variation in $\nu_{\mathrm{T}}(r)$ can be approximated by a quadratic function of r:

$$\nu_{\mathrm{T}}(r) = \nu_{\mathrm{T,peak}} \cdot \left(1 - \frac{r^2}{R_{\mathrm{tube}}^2}\right) \tag{16}$$

Then, the value on the axis $\nu_{\mathrm{T,peak}}$ has been found in *Wolf et al.* [2020a] for several conditions of pressure and flow and for an input power of 1 kW, as the value that best allows to retrieve the experimental peak of T_{g}, obtained from Doppler broadening measurements of the 777 nm atomic oxygen line emission [*Wolf et al.*, 2019]. An improvement is made with respect to the case in *Wolf et al.* [2020a], as the laminar diffusion coefficient in this work is obtained for each species k through a mixture-averaged multicomponent approach, as in *Hirschfelder and Curtiss* [1949]; *Giovangigli* [1990]; *Synek et al.* [2015]:

$$D_{\mathrm{L,k}}(r) = \frac{1 - y_{\mathrm{k}}}{\sum_{l \neq k} \frac{x_{\mathrm{l}}}{\mathcal{D}_{\mathrm{k,l}}}}, \tag{17}$$

where x_{l} is the molar fraction of species l and $\mathcal{D}_{\mathrm{k,l}}$ is the binary diffusion coefficient of the (l, k) pair of species. The binary diffusion coefficients have been computed for all neutral-neutral, ion-neutral and electron-neutral interactions from Chapman-Enskog theory [*Capitelli et al.*, 2013], using the collision integrals in *Laricchiuta et al.* [2009]. In the conditions of this work, in the plasma core region, for ions and neutrals, $D_{\mathrm{L,k}}$ and D_{T} are of the same order of magnitude, around 10^{-2} m^2 s^{-1}.

The MW absorbed power density $P_{\mathrm{abs}}(r)$ is calculated as an output through the steady-state electron energy balance equation [*Alves et al.*, 2018]:

$$P_{\mathrm{abs}}(r) = \left(\frac{P_{\mathrm{el}}}{n_{\mathrm{g}}}(r) + \frac{P_{\mathrm{inel}}}{n_{\mathrm{g}}}(r) + \frac{P_{\mathrm{growth}}}{n_{\mathrm{g}}}(r)\right) n_{\mathrm{g}}(r) n_{\mathrm{e}}(r) + \tag{18}$$

$$\frac{n_{\mathrm{e}}(r)\epsilon(r)v_{\mathrm{z}}(r)}{L} + \frac{d}{dr}\left(-\frac{5}{3}D_{\mathrm{e}}(r)\frac{d}{dr}[n_{\mathrm{e}}(r)\epsilon(r)]\right) ,$$

where P_{el}, P_{inel} and P_{growth} are the components of power lost by electrons through elastic, conservative inelastic and non-conservative inelastic collisions, respectively, calculated from the solver for electron kinetics and dependent on E/n_{g} and gas mixture. ϵ is the mean electron energy also calculated from the electron kinetics solver and D_{e} is the electron diffusion coefficient, calculated from eqs. 14-17. We should notice that the formulation used for the diffusive term in eq. 18 is an approximation based on the assumption of a Maxwellian electron velocity distribution function and an energy-independent momentum-transfer collision frequency [*Alves et al.*, 2018]. However, in the studied conditions, the transport terms (mostly diffusive) in eq. 18 have a weight of the order of only 2% on the calculation of P_{abs}, that is mostly defined by the collisional electron losses. Hence, formulating the transport terms differently would have a negligible effect on $P_{\mathrm{abs}}(r)$.

The electron kinetics solver is the Monte Carlo Flux (MCF) code developed and described in *Vialetto et al.* [2019, 2020], based on the method introduced in *Schaefer and Hui* [1990]. It is used in this model to calculate the power loss terms and the electron mean energy in eq. 18 and the electron-impact rate coefficients that take part in the source term calculations. The MCF code can simulate electrons in any arbitrary gas mixture, including any population of excited states for atoms/molecules. Moreover, it is consistent with the cross sections set for electron impact used in this work. The importance of these considerations for the calculation of rate coefficients has been demonstrated in *Viegas et al.* [2020]; *Vialetto et al.* [2020]. The MCF solution is coupled to the 1D-radial model in a similar way as it was coupled to the zero-dimensional model in *Viegas et al.* [2020]. In 11 equally-spaced positions in the domain, the MCF solution is obtained for 21 values of reduced electric field linearly spaced between 1 and 200 Td. Then, the solution is interpolated in space. As such, the calculated electron parameters are functions of the local E/n_g and of position. The electron kinetics calculations take as input parameters the gas pressure and the frequency of the field, as well as the local gas temperature and composition, consistently with the plasma model and the experimental conditions reported in section 2. The vibrational states of molecules are taken into account in electron collisions by assuming that they are populated according to a Boltzmann distribution at T_g, as in *Viegas et al.* [2020]. The importance of considering these populations for electron kinetics in CO_2 has been demonstrated for example in *Grofulović et al.* [2016]; *Vialetto et al.* [2020]; *Silva et al.* [2020]. The MCF solutions are first obtained for the input molar fractions of the main species CO_2, CO, O_2 and O. Then, after the plasma simulation converges, the MCF solutions are updated and the plasma simulation is run again. The update takes into account the calculated densities of C and of the atomic oxygen excited states, that have influence on the EEDF through both superelastic and stepwise inelastic collisions. As the densities of these species are much lower than those of the main species (whose fractions are fixed) and have only a minor effect on the EEDF, the MCF solutions are updated only once. In this way, electron kinetics is coupled self-consistently with plasma simulations.

The equations in this model are solved with a finite volume discretisation in a uniform grid, where diffusive mass fluxes are discretised using a central difference scheme. These are solved using the Tridiagonal Matrix Algorithm for matrix inversion. Homogeneous Neumann boundary conditions for the radial diffusive fluxes are taken at $r = 0$ and at the tube wall. In this work the 13.5 mm radial domain is divided into 41 cells of 0.33 mm size each. The numerical solution is obtained in a single central processing unit (CPU) with a calculation time ranging typically between 1 and 7 days. One simulation has been performed with 81 cells of 0.17 mm size each and has produced a relative difference in results up to 5% and an increase in calculation time of a factor 5.5, with respect to the same case with 41 cells. The calculation time is mostly due to the MCF calculations taking approximately 11 hours (1 hour per position) and to the very high number of iterations required to fulfil the convergence criteria, which

Resolving discharge parameters from atomic oxygen emission   14

is usually between 2 million and 20 million. On the one hand, the high number of iterations is justified by the use of a small under-relaxation factor of 10^{-5}, necessary for the resolution of the very stiff non-linear system of equations imposed by the complex chemistry in plasmas [*Patankar*, 1980]. On the other hand, we should notice that it is very computationally expensive to simultaneously match n_e with $n_{e,IN}$ in the whole domain, but it is of fundamental importance for the current study of spatial resolution of discharge parameters.

1
2
3
4
5
6
7
8
9
10
...
60

Resolving discharge parameters from atomic oxygen emission   15

3.2. O atom collisional-radiative model in CO_2 conversion plasma

In this section, the reaction scheme used in the model is presented. The reactions considered in *Viegas et al.* [2020] are adopted in this work. These include reactions for neutral thermal chemistry based on the GRI-MECH 3.0 database [*Smith et al.*, 2018] and for charged particle kinetics based on the reaction schemes of *Koelman et al.* [2017]; *Kozák and Bogaerts* [2014]. Charged particle kinetics includes electron-impact ionisation, attachment and dissociation, electron–ion recombination, ion transfers, detachment, ion–ion recombination and associative ionisation. The rate coefficients and electron-impact cross sections considered for those reactions are adopted from *Viegas et al.* [2020]; *Vialetto et al.* [2020]. Electron-electron collisions are not considered, as they are not expected to affect rate coefficients in the conditions of interest beyond an increase of 5%. As in *Viegas et al.* [2020], molecules are vibrationally populated according to a Boltzmann distribution at T_g for which concerns electron kinetics, in agreement with the temperature measurements in *van den Bekerom et al.* [2020]; *van de Steeg et al.* [2020]. Nevertheless, their excited states, as those of C, are not considered for chemical calculations. We thus assume that the radiative emission of O in this plasma is independent of those states and is mostly due to processes affecting exclusively O states. As such, a CRM for atomic oxygen and the excited states listed in table 2 is added in this work, inspired on the recent works of *Caplinger and Perram* [2020] and of *Fiebrandt et al.* [2020]. As in *Viegas et al.* [2020], no wall reactions are considered, since the contracted microwave plasma has no direct interaction with the reactor walls. Together with the reaction scheme in *Viegas et al.* [2020], a total of 225 reactions is considered in our model. The reactions of the CRM are listed in tables 3 and 4 and have been defined according to the following considerations:

- The cross sections for excitation and ionisation of ground-state atomic oxygen by electron impact have been retrieved from *Laher and Gilmore* [1990], where a critical review of experimental and theoretical work on this subject has been presented. Superelastic cross sections are calculated with the formula of Klein-Rosseland [*Capitelli et al.*, 2015], by considering micro-reversibility. The electron kinetics solver considers separate transitions between the ground-state and all the non-Rydberg states and all the Rydberg states with a $O^+(^4S^0)$ core, which is consistent with the set in *Alves et al.* [2016] where all these Rydberg states are lumped together. Rydberg states with $O^+(^2D^0)$ and $O^+(^2P^0)$ cores are taken into account as lumped states, as in *Alves et al.* [2016]. The double ionisation cross section presented in *Laher and Gilmore* [1990] is not considered, due to its very high threshold of around 50 eV.

- The CRM considers that $O(3d\ ^5D^0)$ electron-impact excitation includes the excitation to $O(4s\ ^5S^0)$, $O(4p\ ^5P)$ and $O(4d\ ^5D^0)$, as a way to account for radiative cascading of all quintuplet states above $O(3p\ ^5P)$, as in *Fiebrandt et al.* [2020]. This approach assumes that the upper states relax via radiative processes. The same is done for $O(3d\ ^3D^0)$, including states $O(4s\ ^3S^0)$, $O(4p\ ^3P)$ and $O(4d\ ^3D^0)$. The

Resolving discharge parameters from atomic oxygen emission   16

Nbr.	Reaction	Rate coefficient	Refs.
O1	$e + O(i) \leftrightarrow e + O(j)$	$k(E/n_{\mathrm{g}}, r)$	[1,2,3]
O2	$e + O(i) \rightarrow e + O^+$	$k(E/n_{\mathrm{g}}, r)$	[1]
O3	$e + CO_2 \rightarrow e + CO + O(2p^4\ ^1S)$	$k(E/n_{\mathrm{g}}, r)$	[4]
O4	$e + CO \rightarrow e + C + O(2p^4\ ^1S)$	$k(E/n_{\mathrm{g}}, r)$	[4]
O5	$e + O_2 \rightarrow e + O(2p^4\ ^3P) + O(i)^{\mathrm{a}}$	$k(E/n_{\mathrm{g}}, r)$	[2,4-8]
O6	$e + O_2^+ \rightarrow O(2p^4\ ^3P) + O(2p^4\ ^3P)$	$5.17 \times 10^{-9} \times T_{\mathrm{e}}^{-1}$	[9,10]
O7	$e + O_2^+ \rightarrow O(2p^4\ ^3P) + O(2p^4\ ^1D)$	$1.51 \times 10^{-8} \times T_{\mathrm{e}}^{-0.7}$	[9,11]
R1	$O(3p\ ^5P) \rightarrow O(3s\ ^5S^0)$ [777 nm]	$\tau_{\mathrm{rad1}}^{-1}$	[12-14]
R2	$O(3p\ ^3P) \rightarrow O(3s\ ^3S^0)$ [845 nm]	$\tau_{\mathrm{rad2}}^{-1}$	[12-14]
R3	$O(3d\ ^5D^0) \rightarrow O(3p\ ^5P)$ [926 nm]	$\tau_{\mathrm{rad3}}^{-1}$	[12-14]
R4	$O(3d\ ^3D^0) \rightarrow O(3p\ ^3P)$ [1128 nm]	$\tau_{\mathrm{rad4}}^{-1}$	[12-14]
R5	$O(3d\ ^3D^0) \rightarrow O(2p^4\ ^3P)$ [102 nm]	$\tau_{\mathrm{rad5}}^{-1}$	[12-14]
R6	$O(3s\ ^3S^0) \rightarrow O(2p^4\ ^3P)$ [130 nm]	$\tau_{\mathrm{rad6}}^{-1}$	[12-14]

Table 3. List of atomic oxygen reactions: electron-impact excitation, deexcitation, ionisation and dissociation; electron-ion recombination; and radiative emission taking self-absorption into account. O(i) and O(j) represent any state of atomic oxygen listed in table 2, except when a note is added. The units of rate coefficients for radiative emission are s^{-1}, and for two-body reactions are $\mathrm{cm}^3\ \mathrm{s}^{-1}$. E/n_{g} is the reduced electric field; r is the radial position, corresponding to a local gas mixture and temperature; and T_e is the electron temperature in eV.
References: [1] = *Laher and Gilmore* [1990]; [2] = *Alves et al.* [2016]; [3] = *Barklem* [2007]; [4] = *McConkey et al.* [2008]; [5] = *Erdman and Zipf* [1987]; [6] = *Lawrence* [1970]; [7] = *Itikawa* [2009]; [8] = *Kanik et al.* [2003]; [9] = *Annušová et al.* [2018]; [10] = *Kossyi et al.* [1992]; [11] = *Eliasson and Kogelschatz* [1986]; [12] = NIST database, *Kramida et al.* [2020]; [13] = *Fiebrandt et al.* [2020]; [14] = *Mewe* [1967].
Notes on the states considered: a - $O(2p^4\ ^1D)$, $O(2p^4\ ^1S)$, $O(3s\ ^5S^0)$, $O(3s\ ^3S^0)$, $O(3p\ ^5P)$ and $O(3p\ ^3P)$.

relevance of cascade emission has been put forward by both *Fiebrandt et al.* [2020] and *Caplinger and Perram* [2020].

- Electron-impact collisions with excited states, shown to be relevant in *Caplinger and Perram* [2020], are also considered. The elastic cross sections are considered as being the same as for the ground-state, taken from *Alves et al.* [2016]. The following stepwise excitation collision cross sections have been retrieved from *Barklem* [2007], as in *Caplinger and Perram* [2020]; *Fiebrandt et al.* [2020]: $O(2p^4\ ^1D) \rightarrow O(2p^4\ ^1S)$, $O(3s\ ^3S^0)$, $O(3p\ ^3P)$; $O(2p^4\ ^1S) \rightarrow O(3p\ ^3P)$; $O(3s\ ^5S^0) \rightarrow O(3s\ ^3S^0)$, $O(3p\ ^5P)$, $O(3p\ ^3P)$; $O(3s\ ^3S^0) \rightarrow O(3p\ ^5P)$, $O(3p\ ^3P)$; $O(3p\ ^5P) \rightarrow O(3p\ ^3P)$. They have been calculated in *Barklem* [2007] through a 38-state R-matrix calculation. In the cases where literature sources did not include data tables, cross sections have been digitised from figures. The remaining stepwise excitation and ionisation cross sections are taken as the same as those for electron impact with the ground-state of O from *Laher and Gilmore* [1990]. The same approach to cascade emission is

Resolving discharge parameters from atomic oxygen emission   17

used for stepwise excitation as for ground-state excitation.

- Electron-impact dissociation of CO_2 and CO (reactions O3-O4), using the cross sections in the review of *McConkey et al.* [2008], produce the $O(2p^4\ ^1S)$ state.

- The electron-impact cross sections for dissociation of O_2 into $O(2p^4\ ^3P) + O(2p^4\ ^3P)$ and $O(2p^4\ ^3P) + O(2p^4\ ^1D)$ (reaction O5), which are the most populated states of atomic oxygen, are taken from *Alves et al.* [2016]. Then, for the production of $O(2p^4\ ^1S)$, $O(3p\ ^5P)$ and $O(3p\ ^3P)$ (O5), the dissociative cross sections in *McConkey et al.* [2008] are considered. Finally, we take into account electron-impact dissociation of O_2 into the metastables $O(3s\ ^5S^0)$ and $O(3s\ ^3S^0)$ using the emission cross sections from *Itikawa* [2009]; *Kanik et al.* [2003]. This choice of cross sections is the same as in *Fiebrandt et al.* [2020] and in *Stancu et al.* [2016] and is similar to the one in *Caplinger and Perram* [2020]. While in *Fiebrandt et al.* [2020] a Maxwellian EEDF is assumed to obtain expressions for rate coefficients, in this model we calculate all electron-impact rate coefficients from the EEDF calculated through the MCF method.

- No kinetic data has been found in literature for production of excited states of O from dissociative electron-ion recombination. The exceptions are the reactions listed in *Annušová et al.* [2018] and included in table 3 as O6-O7 for O_2^+ recombination. We should notice that this is the dominant ion in the studied plasma [*Viegas et al.*, 2020].

- The Einstein coefficients for spontaneous emission are taken from the NIST database [*Kramida et al.*, 2020]. Only transitions with Einstein coefficient above 10^5 s^{-1} have been selected (R1-R6 in table 3). The remaining transitions in the NIST database have Einstein coefficient below $10^4\ s^{-1}$ and thus have been neglected. In fact, the emission intensities of the transitions with wavelengths 777 nm, 845 nm and 926 nm (R1-R3) are measured in the experiments in the CO_2 MW plasma reactor. The measurements are not sensitive to the wavelengths of reactions R4-R6, but the importance of these transitions cannot be excluded.

- The influence of self-absorption on transitions R1-R6 is considered as in *Fiebrandt et al.* [2020], where it has been shown to be important. Radiation emitted from a higher level p to a lower level k, of multiplet component l, can be reabsorbed by the lower state to repopulate the higher state. This process limits the number of photons effectively travelling through the plasma. In this work we take it into account by adding a local correction called escape factor $\gamma_{pk,l}(r)$, depending on the number density of the lower level at each position r, such that every coefficient $\tau_{\mathrm{rad}pk}^{-1}(r)$ in table 3 is defined as:

$$\tau_{\mathrm{rad}pk}^{-1}(r) = \sum_l A_{pk,l} \gamma_{pk,l}(r) \frac{g_{p,l}}{\sum_l g_{p,l}}, \tag{19}$$

where $A_{pk,l}$ is the Einstein coefficient of each transition from state p to state k, of multiplet component l, found in NIST; $\gamma_{pk,l}$ is the associated escape factor and $g_{p,l}$ is the statistical weight of the upper state in the corresponding transition. To calculate

Resolving discharge parameters from atomic oxygen emission 　　　　　　　18

$\gamma_{pk,l}$, we use the same approach as in *Fiebrandt et al.* [2020], an approximated empirical formula determined by Mewe [*Mewe*, 1967]. In *Mewe* [1967], the formula assumes homogeneous density profiles of both the upper and the lower state. Then, in *Sushkov et al.* [2013], it has been shown that the approximation is valid with any spatial profile of the states densities, as long as the upper and lower states have similar spatial profiles. It has also been estimated that in the worst case scenario, this empirical formula is approximately a factor of 2–3 off to the correct escape factor. In this work, this method is used due to its simplicity, and, as we use this approximation in the 1D model, we take the local densities at each position r, such that:

$$\gamma_{pk,l}(r) = \frac{2 - exp(-10^{-3}k_{pk,l}(r)\Lambda_{777})}{1 + k_{pk,l}(r)\Lambda_{777}} \tag{20}$$

$$k_{pk,l}(r) = \frac{\lambda_{pk,l}^2}{8\pi}P_{pk,l}(r)\frac{g_{p,l}}{g_{k,l}}n_{k,l}(r)A_{pk,l} \tag{21}$$

$$n_{k,l}(r) = n_k(r)\frac{g_{k,l}}{\sum_l g_{k,l}} \tag{22}$$

$$P_{pk,l}(r) = \lambda_{pk,l}\sqrt{\frac{m_O}{2\pi k_B T_g(r)}} \tag{23}$$

$k_{pk,l}$, $\lambda_{pk,l}$ and $P_{pk,l}$ are the absorption coefficient, the wavelength and the spectral line profile of the associated transition. $P_{pk,l}$ has been taken as in *Fiebrandt et al.* [2017], assuming Doppler broadening as the dominant line broadening mechanism. Λ_{777} is the measured FWHM of the 777 nm emission, here taken as an approximate thickness of the plasma in the radial direction, over which photons are absorbed. m_O is the mass of atomic oxygen, k_B is the Boltzmann constant and $n_{k,l}$ is the number density of species k in the multiplet component l, estimated from the statistical weights $g_{k,l}$.

- Numerical simulations in the conditions studied in this work show that, using the described approach, the effective escape factors can go down to 0.5 in the case of transitions R1-R2 in the centre of the discharge. The escape factors increase radially to approximately 1 on the edges. For transitions R3-R4, with radiative lower state, the escape factor is always close to 1. For the cases of transitions R5-R6, where the lower state is the ground-state, the emission is decreased by about 90% (escape factor of ∼0.1). The approach used in *Santos et al.* [2014] has also been tested, yielding no self-absorption for R1-R4 and complete self-absorption for R5-R6. It has been discarded, since it is only valid for high levels of radiation trapping.

- For the quenching rate coefficients, we use those compiled in *Caplinger and Perram* [2020]. We should notice that many rate coefficients are not reported in literature and many are measured at 300 K only and thus have no temperature dependence. The quenching rate coefficient for excitation transfer Q1 (table 4) is taken from *Dagdigian et al.* [1988], where it has been measured with O_2 as collision partner from the ratio of the 777 nm and 845 nm emission intensities. The important role of this reaction has been put forward in *Caplinger and Perram* [2020]. As this rate

coefficient hasn't been found in literature for the other collision partners (CO_2, CO, O and C), we have taken the same rate coefficient for all collision partners. In *Morillo-Candas et al.* [2019], the quenching rate coefficient of reaction $O(3p\ ^5P)$ + $M \rightarrow O(2p^4\ ^3P)$ + M, has been measured in low pressure DC glow discharges in O_2 and in CO_2 from the analysis of the temporal decay of fluorescence signals. It has been found to have very similar values in the different mixtures, which reinforces our assumption of assuming the same rate coefficient for different collision partners. Moreover, we have assumed the same rate coefficient for reactions Q1 and Q2, due to the similarity of the states involved.

- For the quenching reactions of $O(2p^4\ ^1D)$ and $O(2p^4\ ^1S)$ (Q3-Q8), the rate coefficients used in the model of *Gordiets et al.* [1995] are taken. The coefficients for collision partners CO and CO_2 are considered as being the same as for O_2, according to the same reasoning followed for Q1. When C is the collision partner, the rate coefficients for N or N_2 quenchers is taken. We should notice that C has a low molar fraction in the current study, when compared to the other neutrals.

- The quenching rate coefficients of the higher metastable $O(3s\ ^5S^0)$ (Q9-Q13) are taken from *Mori et al.* [1992], where they have been measured for O_2, CO, CO_2 and N_2 quenchers from absorption decay curves. For O and C quenchers, the coefficients from O_2 and N_2 are considered, respectively. Furthermore, we assume the rate coefficients for the remaining metastable $(3s\ ^3S^0)$ to be equal to those for $O(3s\ ^5S^0)$, as in *Caplinger and Perram* [2020].

- Finally, for the quenching of the radiative states (Q14-Q16), the quenching coefficients with O_2 are considered, measured for $O(3p\ ^5P)$ in *Dagdigian et al.* [1988] and for $O(3p\ ^3P)$ in *Niemi et al.* [2001]. As for the other quenching reactions, we assume the same rate coefficient for O_2 quencher and for CO_2, CO and O quenchers. For C quencher, the coefficient with N_2 quencher measured in *Niemi et al.* [2001] is taken for all radiative states.

- A simple sensitivity analysis study has been performed on the quenching rate coefficients. Simulations have been run while replacing a few quenching coefficients by the corresponding ones from different sets [*Dagdigian et al.*, 1988; *Pietanza et al.*, 2020; *Fiebrandt et al.*, 2020]. It has been verified that this leads to no relevant difference in the simulation results in this work, which suggests that an eventual temperature dependence of these coefficients would not affect the conclusions obtained in this work.

Resolving discharge parameters from atomic oxygen emission   20

Nbr.	Reaction	Rate coefficient	Refs.
Q1	$O(3p\ ^3P) + M \rightarrow O(3p\ ^5P) + M$	6×10^{-11}	[15,16]
Q2	$O(3d\ ^3D^0) + M \rightarrow O(3d\ ^5D^0) + M$	6×10^{-11}	[15,16]
Q3	$O(2p^4\ ^1D) + M^b \rightarrow O(2p^4\ ^3P) + M^b$	$2.6 \times 10^{-11} \times \exp^{67/T_g} + 10^{-12}$	[15,17]
Q4	$O(2p^4\ ^1D) + O \rightarrow O(2p^4\ ^3P) + O$	8×10^{-12}	[15,17]
Q5	$O(2p^4\ ^1D) + C \rightarrow O(2p^4\ ^3P) + C$	2.3×10^{-11}	[15,17]
Q6	$O(2p^4\ ^1S) + M^b \rightarrow O(2p^4\ ^3P) + M^b$	$4 \times 10^{-12} \times \exp(-865/T_g)$	[15,17]
Q7	$O(2p^4\ ^1S) + O \rightarrow O(2p^4\ ^1D) + O(2p^4\ ^1D)$	$5 \times 10^{-11} \times \exp(-301/T_g)$	[15,17]
Q8	$O(2p^4\ ^1S) + C \rightarrow O(2p^4\ ^3P) + C$	10^{-12}	[15,17]
Q9	$O(i)^c + O_2 \rightarrow O(2p^4\ ^3P) + O_2$	2.2×10^{-10}	[15,18]
Q10	$O(i)^c + CO_2 \rightarrow O(2p^4\ ^3P) + CO_2$	5.3×10^{-10}	[15,18]
Q11	$O(i)^c + CO \rightarrow O(2p^4\ ^3P) + CO$	8.3×10^{-11}	[15,18]
Q12	$O(i)^c + O \rightarrow O(2p^4\ ^3P) + O$	2.2×10^{-10}	[15,18]
Q13	$O(i)^c + C \rightarrow O(2p^4\ ^3P) + C$	3.5×10^{-11}	[15,18]
Q14	$O(i)^d + M^e \rightarrow O(2p^4\ ^3P) + M^e$	10.8×10^{-10}	[15,16]
Q15	$O(i)^f + M^e \rightarrow O(2p^4\ ^3P) + M^e$	9.3×10^{-10}	[15,19]
Q16	$O(i)^g + C \rightarrow O(2p^4\ ^3P) + C$	5.9×10^{-10}	[15,19]

Table 4. List of atomic oxygen quenching reactions. $O(i)$ and $O(j)$ represent any state of atomic oxygen listed in table 2 and M represents any neutral species, except when a note is added. The units of rate coefficients are $cm^3\ s^{-1}$. T_g is the gas temperature in K.

References: [15] = *Caplinger and Perram* [2020]; [16] = *Dagdigian et al.* [1988]; [17] = *Gordiets et al.* [1995]; [18] = *Mori et al.* [1992]; [19] = *Niemi et al.* [2001].

Notes on the species or states considered: b - CO_2, CO and O_2; c - $O(3s\ ^5S^0)$ and $O(3s\ ^3S^0)$; d - $O(3p\ ^5P)$ and $O(3d\ ^5D^0)$; e - CO_2, CO, O_2 and O; f - $O(3p\ ^3P)$ and $O(3d\ ^3D^0)$; g - $O(3p\ ^5P)$, $O(3p\ ^3P)$, $O(3d\ ^5D^0)$ and $O(3d\ ^3D^0)$.

4. Results

In this section, we apply the model previously described to the different plasma conditions A, B and C explained in section 2.2. Firstly, the initial assumptions of $n_e(r)$ are used. The relationship between $n_e(r)$ and $I_{777}(r)$ is obtained from simulation results and used to correct the input profile of $n_e(r)$ consistently with the measured Gaussian profile of $I_{777}(r)$. This process is explained in detail for the low-confinement discharge of condition A, for which several spatially-resolved discharge parameters are provided from the simulation results. Then, the same procedure is applied to the high-confinement discharge of condition B and to the wider parameter range of set C. In the case of set C, it is shown that the findings from this study have a direct impact on the flow simulations that provide input T_g and composition, and hence the flow model and the procedure to correct spatial profiles of discharge parameters are interdependent. Overall, this study allows both to quantify the impact of parameter changes in the relationships between discharge parameters, and to generalise certain conclusions about the spatial resolution of those parameters and its potential impacts on the study of plasmas for CO_2 conversion.
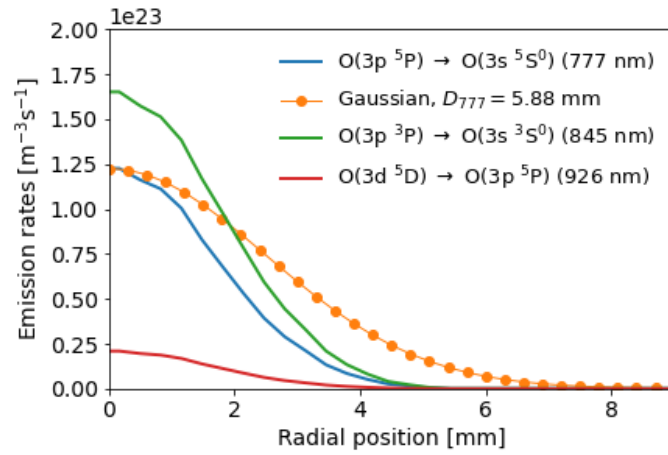
4.1. Condition A: low-confinement discharge

4.1.1. Using initial assumptions
We start by using the plasma model to study the low-confinement discharge of condition A, described in section 2.2. The assumption that $n_e(r)$ follows the same Gaussian profile as the measured $I_{777}(r)$ (eq. 8) is taken as a starting point for the model input. Figure 4 depicts the emission rates of the three transitions identified in experiments (R1-R3 in table 3), obtained as simulation results, which have the same FWHM as the corresponding emission intensities. A Gaussian profile with the same peak as the simulated 777 nm emission rate and with the measured FWHM, $\Lambda_{777} = 5.88$ mm, is added, for comparison with the simulation results.

The results in figure 4 show that the numerically-obtained emission rates have seemingly Gaussian radial profiles, as in the experiments. Moreover, the ratios between the three emission rates agree qualitatively with experimental measurements. However, it is visible that the simulated emission rate of the 777 nm transition has a narrower radial profile than the measured emission intensity. This result suggests that the initial assumption on input $n_e(r)$ (linearly proportional to $I_{777}(r)$) is incorrect. Indeed, the input taken from eq. 8 assumes that n_e and I_{777} are linearly proportional. In figure 5, the dependence of the three considered emission rates on n_e is presented. The simulation results have been fitted in order to derive the proportionality parameter s from eq. 5, and we found the best fits to result from polynomial functions of second order. The fits are included in figure 5. According to these fits, the emission rates of the 777, 845 and 926 nm transitions, respectively, R_{777}, R_{845} and R_{926}, are given in $\mathrm{m}^{-3}\mathrm{s}^{-1}$ by:

$$R_{777}(n_e) = -2259[\mathrm{s}^{-1}] \times n_e[\mathrm{m}^{-3}] + 1.731 \times 10^{-15}[\mathrm{m}^3\mathrm{s}^{-1}] \times n_e^2[\mathrm{m}^{-6}] \quad (24)$$

Resolving discharge parameters from atomic oxygen emission   22

Figure 4. Radial profiles of the simulated emission rates corresponding to the radiative transitions of wavelength 777, 845 and 926 nm, for condition A (950 W, 9 slm and 100 mbar). A Gaussian curve with the measured Λ_{777} is also presented.

$$R_{845}(n_e) = -1308[\text{s}^{-1}] \times n_e[\text{m}^{-3}] + 2.161 \times 10^{-15}[\text{m}^3\text{s}^{-1}] \times n_e^2[\text{m}^{-6}] \quad (25)$$

$$R_{926}(n_e) = -516.5[\text{s}^{-1}] \times n_e[\text{m}^{-3}] + 3.076 \times 10^{-16}[\text{m}^3\text{s}^{-1}] \times n_e^2[\text{m}^{-6}] \quad (26)$$
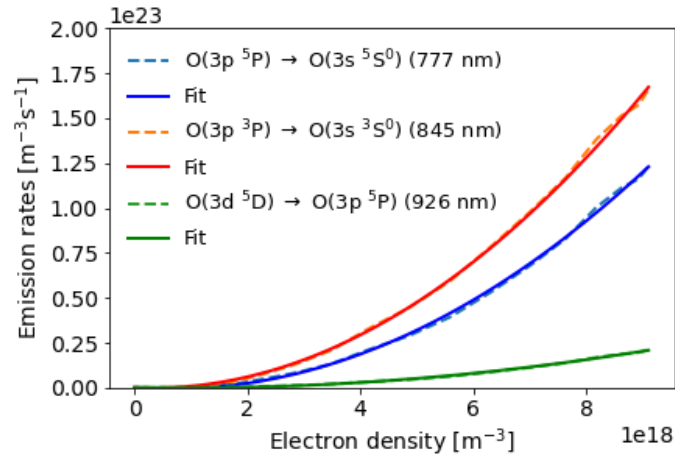
Figure 5. Emission rates corresponding to the radiative transitions of wavelength 777, 845 and 926 nm, as function of n_e, for condition A (950 W, 9 slm and 110 mbar). Simulation results and polynomial fits.

Figure 5 shows that the polynomial functions provide good fits to the simulation results. Furthermore, it is demonstrated that the dependence of the emission rates on n_e is not linear, but rather closer to quadratic, and thus the assumption taken on the profile of $n_e(r)$ should be corrected. This dependence will be explained in the next paragraphs, after correcting the input profile of $n_e(r)$.

Resolving discharge parameters from atomic oxygen emission 23

4.1.2. Corrections to assumptions

The assumption on $n_e(r)$ that is taken as input in the model can be corrected based on the fits shown previously. Indeed, as we have described $R_{777}(n_e)$ as a polynomial of second order, n_e can also be described as a polynomial of second order of $R_{777}^{1/2}$, with fitting parameters c_1 and c_2, of the form:

$$n_e = c_1 \times R_{777}^{1/2} + c_2 \times R_{777} \tag{27}$$

By assuming $R_{777}(r)$ to follow a Gaussian profile of FWHM Λ_{777} and characteristic width σ_{777} (eq. 1), and then line-integrating eq. 27 considering the measured $n_{e\Lambda}$, we obtain:

$$n_{e\Lambda} = c_1 \times R_{777}^{1/2}(0)\sqrt{4\pi}\sigma_{777} + c_2 \times R_{777}(0)\sqrt{2\pi}\sigma_{777} \tag{28}$$

$R_{777}(0)$ can be directly obtained from this equation. Then, eq. 27 yields a new profile for $n_e(r)$, that consists of a superposition of two Gaussian curves of different FWHM and that stems directly from the simulation results using the previous assumption for $n_e(r)$. We should notice that n_{e0} of the new profile is different than the one firstly assumed, but the measured line-integral $n_{e\Lambda}$ is conserved. In the case of condition A using the initial assumption for $n_e(r)$, the simulation results yield $c_1 = 3.097 \times 10^7$ m$^{-3/2}$s$^{1/2}$ and $c_2 = -1.861 \times 10^{-5}$ s. Using these values, a new profile of $n_e(r)$ is used as input for the simulations. Then, as the second iteration of simulation results does not yet provide an agreement of the $R_{777}(r)$ profile with experiments within 5%, this procedure is repeated until that condition is satisfied. For the case of condition A, 3 simulations were required to find a satisfying $R_{777}(r)$ profile. The succeeding $n_e(r)$ and $R_{777}(r)$ profiles are presented in figure 6.
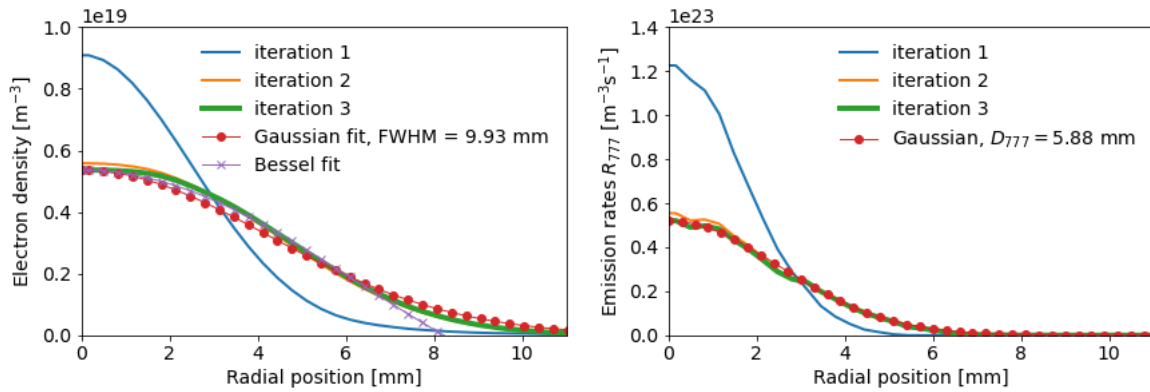
Figure 6. Radial profiles of n_e (on the left) and R_{777} (on the right) for successive iterations, for condition A (950 W, 9 slm and 110 mbar). Each iteration corresponds to a different input $n_e(r)$. A Gaussian function and a Bessel function have been fitted to the last profile of $n_e(r)$. A Gaussian curve with experimentally-obtained Λ_{777} is also compared to the last result of $R_{777}(r)$.

As we can notice from figure 6, the applied correction procedure results in a broadening of the input $n_e(r)$ and of the output $R_{777}(r)$, until the emission rate approximately matches a Gaussian curve with FWHM of Λ_{777}, the one measured for

emission intensity. This procedure is proven to successfully reproduce the measured radial profile of R_{777}. As such, this model can radially resolve discharge parameters. In fact, the $n_e(r)$ profile that matches the measured output can be approximately described as a Gaussian profile with FWHM = 9.93 mm, *i.e.*, with a FWHM value 1.69 times higher than the one of R_{777}. Consequently, as $n_{e\Lambda}$ is conserved in eq. 6, the peak n_{e0} is lower than initially assumed, by approximately the same factor of 1.69. Following eq. 2, the proportionality parameter s is calculated as $1.69^2 \simeq 2.85$, close to the stated upper limit of 2. The fact that $n_e(r)$ follows a seemingly Gaussian profile agrees with previous studies of contracted discharges at intermediate to high pressures in *Petrov and Ferreira* [1999]; *Martinez et al.* [2004]; *Kabouzi et al.* [2007]; *Dyatko et al.* [2008]; *Golubovskii et al.* [2011]; *Shneider et al.* [2014]; *Golubovskii et al.* [2017]; *Ridenti et al.* [2018]; *Zhong et al.* [2019]. Furthermore, we find n_e to have a broader radial profile than the emission intensity, which consists in the phenomenon of optical contraction reported in *Golubovskii et al.* [2011, 2020]. It is also visible in figure 6 that, besides the Gaussian fit, $n_e(r)$ can also be fitted by a Bessel function or by a paraboloidal function (not shown), in agreement with the radially-resolved n_e Thomson scattering measurements in the argon MW discharge in *Carbone et al.* [2012]. However, unlike the Gaussian fit, these functions become negative well before reaching the walls, which is not compatible with the presence of diffusive transport. As such, we deem it more fit to describe the radial profiles of n_e as Gaussian functions.

Resolving discharge parameters from atomic oxygen emission   25

4.1.3. Kinetics of O emission intensity

To understand the proportionality parameter s around 2.85, the main reaction rates of production and destruction of the upper state of the 777 nm transition, O(3p ^{5}P), are presented in figure 7, from the simulation results of iteration 3.
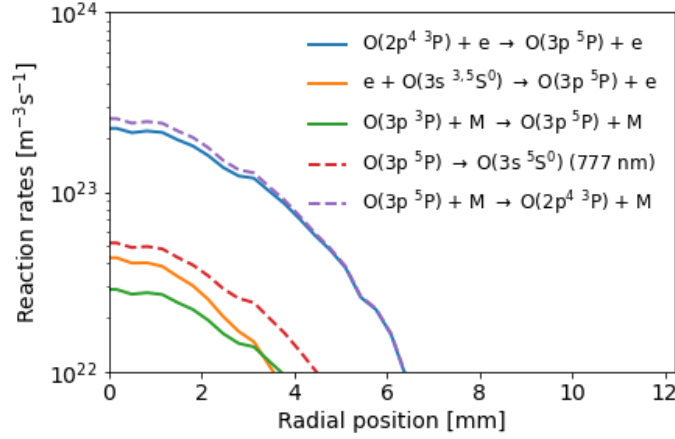
Figure 7. Radial profiles of the main rates of source and loss of the upper radiative state of the 777 nm transition, O(3p ^{5}P), for condition A (950 W, 9 slm and 110 mbar). Production rates in solid lines and loss rates in dashed lines. Simulation results from iteration 3.

Figure 7 shows that the main production reactions of O(3p ^{5}P) are electron-impact reactions, firstly through electron impact with the ground-state of atomic oxygen, and then through collisions with the higher metastables O(3s ^{5}S^0) and O(3s ^{3}S^0). This result highlights the relevance of stepwise excitation put forward in *Caplinger and Perram* [2020] and shown for O(3p ^{3}P) in *Fiebrandt et al.* [2020]. Quenching from upper states (reaction Q1 in table 4) and emission from upper states (R3, not shown in figure 7) also populate O(3p ^{5}P), although this last reaction contributes to less than 5% of production. Therefore, cascade emission populating the upper states also influences the production of O(3p ^{5}P), as highlighted in both *Fiebrandt et al.* [2020] and *Caplinger and Perram* [2020]. Other production mechanisms of O(3p ^{5}P) that have been considered in the simulations, such as dissociative excitation and other electron-impact reactions, appear to play a negligible role. As far as losses are concerned, the main mechanisms are quenching and radiative emission. Radiation self-absorption has a role in these simulations, confirming the importance attributed to it in *Fiebrandt et al.* [2020]. Indeed, the emission coefficient τ_{rad}^{-1} of the 777 nm transition in condition A is a function of r. τ_{rad}^{-1} is 3.38×10^7 s^{-1} at $r = 0$ and increases to its natural value of 3.69×10^7 s^{-1} for $r > 5$ mm. Other loss processes of O(3p ^{5}P) included in the model, through transport (convective and diffusive) and electron impact, are shown to have a lesser role for O(3p ^{5}P) balance. Overall, we can say that hypothesis 1 in section 2.1 on the 777 nm radiation balance is approximately verified, as it correctly estimates the importance of direct electron-impact excitation, quenching and emission from O(3p ^{5}P), but neglects the secondary role of stepwise excitation and of the states above O(3p ^{5}P).

Resolving discharge parameters from atomic oxygen emission 26

Hypothesis 2 is also approximately verified, although τ_{rad}^{-1} is not radially homogeneous. Indeed, quenching is the main loss process ($n_{\mathrm{g}} k_{\mathrm{Q}} > \tau_{\mathrm{rad}}^{-1}$) and k_{Q} is approximately radially homogeneous. Thus, if we consider an effective electron-impact excitation coefficient $k_{\mathrm{eff}}(T_{\mathrm{e}})$ including stepwise excitation, we can write:

$$I_{777} \propto \tau_{\mathrm{rad}}^{-1} \; n_{\mathrm{e}} \; x_{\mathrm{O}} \; k_{\mathrm{eff}}(T_{\mathrm{e}}) \tag{29}$$

In the plasma, as we approach the centre, n_{e} increases and τ_{rad}^{-1} slightly decreases. Then, in figure 8, we evaluate the radial dependence of T_{e} (2/3 of the electron mean energy), of E/n_{g} and of the electric field magnitude E, as well as the dependence of the electron-impact excitation coefficient on n_{e}. The impact of stepwise excitation is highlighted by depicting both the ground-state electron-impact excitation coefficient to O(3p ^{5}P), k_{exc}, and the effective coefficient including also excitation from the higher metastables, k_{eff}.
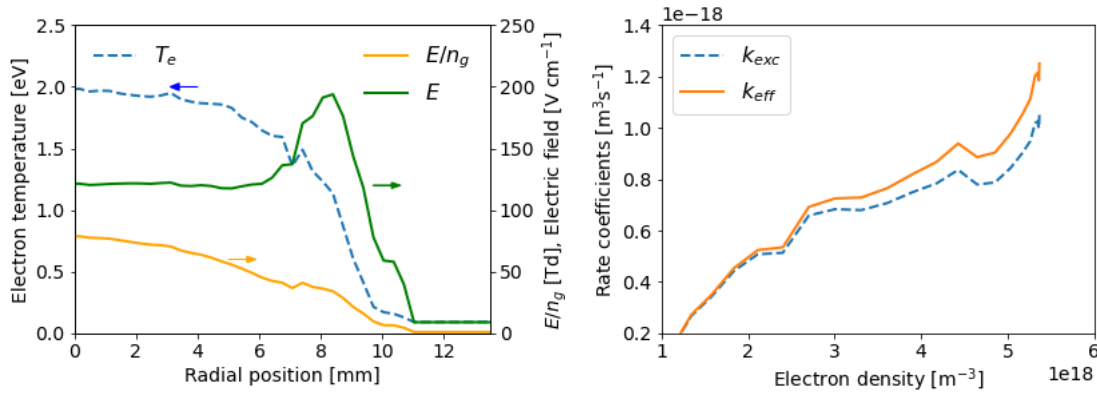
Figure 8. On the left, radial profiles of T_{e}, E/n_{g} and E. On the right, electron-impact excitation coefficients of O(3p ^{5}P), as function of n_{e}. k_{exc} is the coefficient corresponding to excitation from ground-state only. k_{eff} is an effective coefficient, corresponding to excitation from ground-state O(2p^4 ^{3}P), O(3s ^{5}S^0) and O(3s ^{3}S^0). Simulation results from iteration 3.

The simulation results in figure 8 indicate that T_{e} and E/n_{g} in the CO$_2$ MW discharge have concave shapes as in the studies of contracted discharges in *Kabouzi et al.* [2007]; *Gregório et al.* [2010]; *Golubovskii et al.* [2011]; *Gregório et al.* [2012]; *Golubovskii et al.* [2017]; *Ridenti et al.* [2018]; *Zhong et al.* [2019]; *Golubovskii et al.* [2020], due to the self-reinforcing cycle between heating and electron-driven collisionality. However, here the electric field magnitude presents a rather flat profile in the whole plasma region up to $r = 10$ mm. We should notice that for higher radial positions, where $n_{\mathrm{e}}(r) \le 7 \times 10^{16}$ m^{-3} and no electron-impact ionisation takes place, the simulation result of E/n_{g} is assumed to have a minimum value of 1 Td, which also affects the calculation of T_{e} and E. Conversely, in the 3D electromagnetic simulation results in *Groen et al.* [2019], addressing a low-confinement discharge in the same MW reactor and assuming eq. 8 as input profile, E/n_{g} and E have rather flat profiles only in the first 4 mm near the axis, and then a convex shape radially outwards. Moreover, the values of E/n_{g} and E reported in that work are close to twice as much as those shown here. These discrepancies and

the importance of the current study for the results in *Groen et al.* [2019] are discussed in section 4.4.

Figure 8 also shows that, as E/n_{g} increases towards the axis where n_{e} is also higher, the electron-impact excitation coefficients increase almost linearly with n_{e}. The increase of k_{exc} and k_{eff} is expected in the context of contracted discharges where gas heating and electron-driven collisionality reinforce each other and where the electron-impact ionisation coefficient also needs to increase to maintain a higher n_{e} [*Viegas et al.*, 2020]. This relationship means that the main production channels of O(3p ^{5}P) cannot be considered radially homogeneous, which invalidates hypothesis 3 in section 2.1. It also shows that the concave shape of both E/n_{g} and n_{e} is the main reason for the optical contraction phenomenon observed in this work, which is in agreement with the analysis reported in *Golubovskii et al.* [2020] concerning helium glow discharges.

The last element to analyse in eq. 29 is the molar fraction of atomic oxygen x_{O}, that has been measured and shown to have a concave profile in figure 2. If we consider a plasma region of 5.1 mm radius where n_{e} is halved (figure 6), x_{O} drops radially in the same region also by approximately a factor 2 (figure 2). Indeed, n_{e} and x_{O} have rather similar radial profiles. As assumed in hypothesis 4, x_{O} is defined by thermal chemistry and charged particle kinetics, in addition to a contribution of transport which remains largely unknown in this reactor. Hence, the large radial variations of T_{g} justify the approximately linear correlation between n_{e} and x_{O}. This assessment allows to explain, from eq. 29, why the proportionality parameter s between I_{777} and n_{e} is found to be close to 2.85. As the radial position approaches the centre and n_{e} increases, although τ_{rad}^{-1} slightly decreases, x_{O} and k_{eff} increase proportionally to n_{e}, justifying a proportionality parameter between 2 and 3. We should notice that this conclusion holds despite the experimental uncertainty in input parameters, as the proportionality between emission intensity and n_{e} is mostly dependent on the shape of radial profiles, which is independent of the absolute value of $n_{\mathrm{e}\Lambda}$ and of the relatively low experimental uncertainties in T_{g} and composition.

Resolving discharge parameters from atomic oxygen emission 28

4.1.4. Power density profile

Another very important parameter for MW discharge characterisation that is affected by the optical contraction, due to its proximity to n_e, is the absorbed power density, P_{abs}. In figure 9 we assess the radial profile of $P_{abs}(r)$, calculated according to eq. 18.
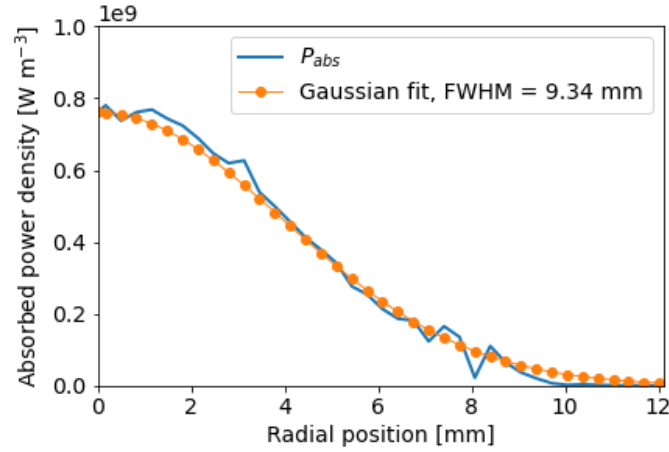

Figure 9. Radial profile of absorbed power density for condition A (950 W, 9 slm and 110 mbar) and Gaussian fit. Simulation results from iteration 3.

Figure 9 shows that $P_{abs}(r)$ can also be approximated as a Gaussian curve for condition A, with a FWHM $\Lambda_{P_{abs}} = 9.34$ mm, very close to the one of n_e. Indeed, we find a FWHM 1.59 times higher than Λ_{777} and thus a proportionality $I_{777} \propto P_{abs}^{s_p}$, $s_p \simeq 2.5$. Following eq. 18, and considering that the electron transport terms have a weight of only 2% on the calculation of P_{abs}, we can write $P_{abs}(r) \simeq \left(\frac{P_{el}}{n_g}(r) + \frac{P_{inel}}{n_g}(r) + \frac{P_{growth}}{n_g}(r) \right) n_g(r) n_e(r)$. We should notice that the collisional electron losses increase with E/n_g and thus also with n_e, but n_g is inversely correlated with n_e. These relationships justify a similar but lower proportionality parameter between I_{777} and P_{abs} than between I_{777} and n_e for condition A. The results in this section show that it is relevant to correct the assumptions on the proportionality between I_{777}, n_e and P_{abs}. Moreover, it is demonstrated that we can successfully resolve discharge parameters from I_{777} and the proposed procedure, for the case of a low-confinement discharge.

4.2. Condition B: high-confinement discharge

The confinement degree of the CO_2 MW discharge depends strongly on input power and pressure [*Wolf et al.*, 2020b]. In this section, we evaluate whether the conclusions taken from the study of condition A can be extended to conditions of high-confinement discharges. Starting from the input profile of $n_e(r)$ described in section 2.2, the same correction procedure used for condition A is applied to condition B. After one correction, the $R_{777}(r)$ and $n_e(r)$ profiles represented in figure 10 are obtained. Two Gaussian curves are added to the figure: one with the simulated peak of R_{777} and the measured FWHM Λ_{777}, and one as a fit to the $n_e(r)$ profile.
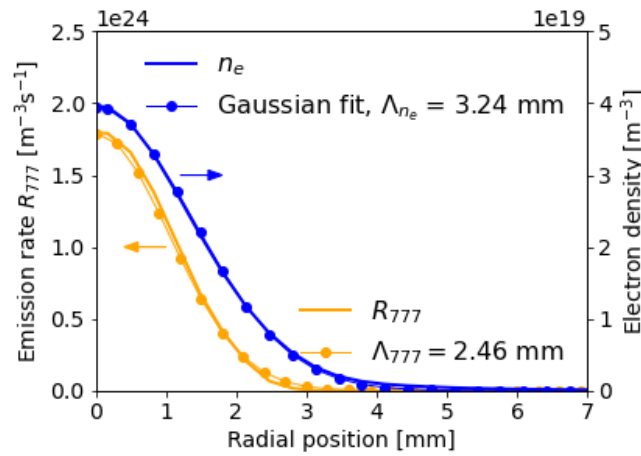

Figure 10. Radial profiles of the 777 nm transition emission rate (left-side axis) and the corrected electron density (right-side axis) for condition B (860 W, 12 slm and 150 mbar). The simulation results after correction procedure and the Gaussian curves with measured FWHM Λ_{777} and fitted FWHM Λ_{n_e} are presented.

Similarly to condition A, figure 10 shows that an approximately Gaussian R_{777} radial profile is obtained with the experimental Λ_{777} as FWHM, in the high-confinement condition B. Indeed, the correction procedure we developed is successful in reproducing the experimental profiles for different conditions of power, pressure and confinement degree. The radial profile of n_e is obtained as a Gaussian curve of FWHM $\Lambda_{n_e} > \Lambda_{777}$, which confirms the phenomenon of optical contraction. The ratio $\Lambda_{n_e}/\Lambda_{777}$ for condition B is 1.32 and the proportionality parameter s between n_e and I_{777} ($I_{777} \propto n_e^s$) is 1.74, lower than the corresponding values for condition A (1.69 and 2.85, respectively). The relationship between n_e and I_{777} is also described by eq. 29 in condition B, as the main reaction mechanisms for the balance of $O(3p\ ^5P)$ are the same as for condition A. However, we should notice that stepwise excitation to $O(3p\ ^5P)$ has a more important role in high-confinement conditions. Following eq. 29, the difference in s between conditions A and B is justified by the different behaviour of τ_{rad}^{-1} and of x_O between these discharges. In fact, the electron-impact excitation coefficient to $O(3p\ ^5P)$ is approximately linearly proportional to n_e in both conditions A and B. T_e and E/n_g are concave and E is approximately flat within the plasma in both contracted modes.

Resolving discharge parameters from atomic oxygen emission   30

In the case of condition B, T_e and E/n_g have maxima of 2.4 eV and 110 Td, and $E \simeq 140$ V cm^{-1} for $r < 3$ mm, higher values than for condition A. Contrarily to the low-confinement discharge, these values should not be compared to those found for a high-confinement discharge in *Groen et al.* [2019] since significantly higher pressure and lower temperature are considered in that work. The lower proportionality parameter s in the high-confinement condition is justified mostly by the more homogeneous x_O profile revealed in the measurements presented in figure 3. x_O is close to 0.4 for $r < 3$ mm and decreases to 0.2 at $r = 5$ mm, while n_e decreases by two orders of magnitude along the same distance. Moreover, the emission coefficient τ_{rad}^{-1} evolves inversely to n_e, as it falls linearly from its original value of 3.69×10^7 s^{-1} for $r > 4$ mm to 2×10^7 s^{-1} at $r = 0$, due to the higher self-absorption in high-confinement conditions. Finally, the simulated power density is also fitted to a Gaussian curve, as shown in figure 11.
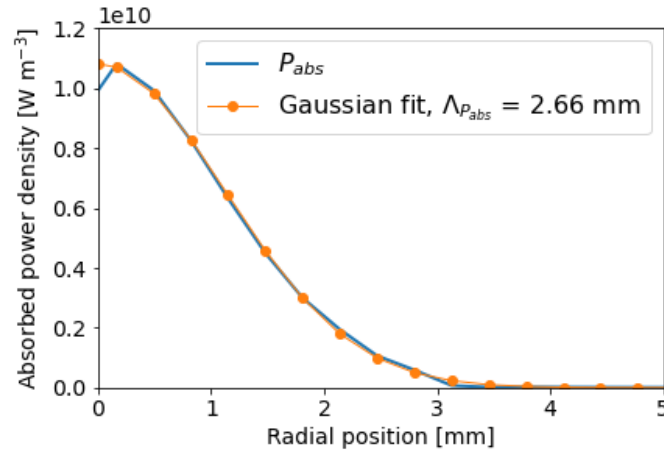

Figure 11. Radial profile of simulated absorbed power density for condition B (860 W, 12 slm and 150 mbar) and Gaussian fit.

Figure 11 shows that the Gaussian curve describing $P_{abs}(r)$ for condition B has $\Lambda_{P_{abs}} = 2.66$ mm, very close to Λ_{777}. Indeed, we find $\Lambda_{P_{abs}}/\Lambda_{777} = 1.08$ and thus $s_p = 1.16$, very close to the initial assumption of $s_p = 1$ (hypothesis 6 in section 2.1). Furthermore, figure 9 shows a dip in the simulated $P_{abs}(r)$ in the axis of the discharge. As noted in the study of condition A, following the electron energy equation (eq. 18), collisional electron losses increase with E/n_g and thus also with n_e, but n_g is inversely correlated with n_e. The sharp gradients of T_g and n_g in high-confinement conditions help explain both the dip in P_{abs} and $\Lambda_{P_{abs}} \ll \Lambda_{n_e}$.

The conclusions from the study of condition A on the most relevant factors to take into account to relate I_{777} and n_e are kept when changing power, pressure and confinement degree in condition B. However, it is shown here that the proportionality between I_{777}, n_e and P_{abs} is not the same in every plasma, as n_e, T_g and x_O have significantly different profiles according to the confinement degree. Hence, different plasma conditions require dedicated analysis in order to spatially resolve discharge parameters.

Resolving discharge parameters from atomic oxygen emission 31

4.3. Set of conditions C: interdependence with flow modelling

In the set of conditions C, described in section 2.2, the input of T_{g} and composition used to resolve discharge parameters is obtained from flow simulations of the model described in *Wolf et al.* [2020a]. The observed confinement degree in these conditions generally stands between the one of the low-confinement discharge of condition A and that of the high-confinement discharge of condition B. The values and extension of T_{g} and dissociation degree are also in between those of the two previously studied conditions. As such, by applying the same correction procedure as in the previous sections, we expect to obtain, for the set of conditions C, spatial profiles and proportionality parameters s and s_{p} in between those found for conditions A and B. Indeed, the Gaussian radial profiles of R_{777} with experimentally-measured Λ_{777} have been obtained for this set of conditions with 3 or 4 iterations of the assumed $n_{\mathrm{e}}(r)$ profiles. As a result, corrected profiles of $n_{\mathrm{e}}(r)$ and $P_{\mathrm{abs}}(r)$ have been retrieved. While $n_{\mathrm{e}}(r)$ is well described by a single Gaussian curve, $P_{\mathrm{abs}}(r)$ for the set of conditions C slightly deviates from this shape, due to the dip at the axis that has been discussed for condition B, and whose depth increases with pressure. Still, the profiles $P_{\mathrm{abs}}(r)$ have been fitted to Gaussian functions with FWHM $\Lambda_{\mathrm{P}_{\mathrm{abs}}}$. In figure 12, Λ_{777}, $\Lambda_{n_{\mathrm{e}}}$ and $\Lambda_{\mathrm{P}_{\mathrm{abs}}}$ are compared as function of pressure, and the ratios between these quantities are represented for the set of conditions C.
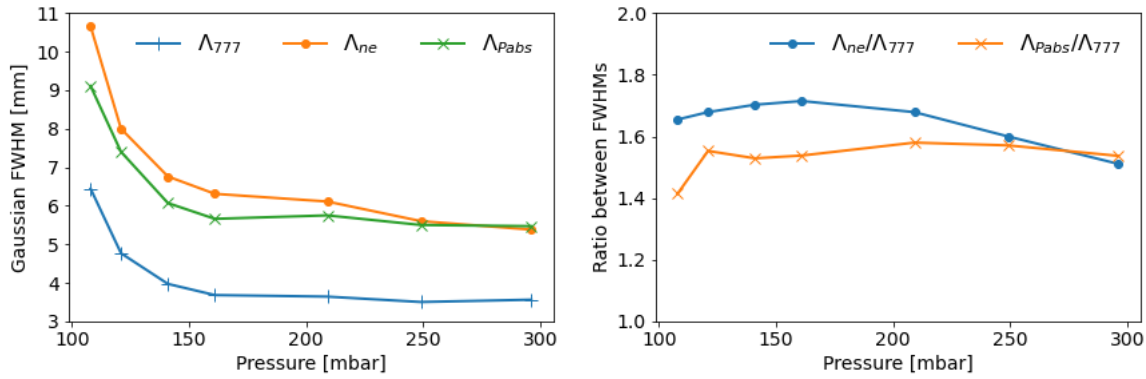

Figure 12. On the left, different diameters as function of pressure, after applying the correction procedure. On the right, the ratios between $\Lambda_{n_{\mathrm{e}}}$ and Λ_{777} and between $\Lambda_{\mathrm{P}_{\mathrm{abs}}}$ and Λ_{777}, as function of pressure. Results obtained for the set of conditions C.

Figure 12 shows that $\Lambda_{n_{\mathrm{e}}}$ and $\Lambda_{\mathrm{P}_{\mathrm{abs}}}$ are, as Λ_{777}, approximately independent of pressure for pressures above 150 mbar, confirming the conclusion from *Wolf et al.* [2019] that $\Lambda_{n_{\mathrm{e}}}$ is independent of pressure in H-mode conditions. Both $\Lambda_{n_{\mathrm{e}}}$ and $\Lambda_{\mathrm{P}_{\mathrm{abs}}}$ are higher than Λ_{777}, as the discharge is in every case broader than initially assumed. For the set of conditions C, $\Lambda_{n_{\mathrm{e}}}/\Lambda_{777}$ varies between 1.45 and 1.73 and $\Lambda_{\mathrm{P}_{\mathrm{abs}}}/\Lambda_{777}$ stands between 1.42 and 1.58. We should notice that the correction procedure leads to a decrease of $n_{\mathrm{e}0}$ relative to the initial assumption in the same proportion as the increase in $\Lambda_{n_{\mathrm{e}}}$. $P_{\mathrm{abs}0}$ also decreases with the correction procedure, but in a different proportion with respect to $\Lambda_{\mathrm{P}_{\mathrm{abs}}}$, since it is a simulation result and no line-integrated conservation is imposed

as in the case of n_e. In fact, P_{abs0} decreases by a factor between 1.6 (for 296 mbar) and 4.7 (for 108 mbar). The values of the ratios $\Lambda_{n_e}/\Lambda_{777}$ and $\Lambda_{P_{abs}}/\Lambda_{777}$ are very close to those found in the case of the low-confinement discharge in condition A as, following eq. 29, x_O and k_{eff} are approximately linearly proportional to n_e, and τ_{rad}^{-1} is convex in the plasma region. We should notice that the $x_O(r)$ profile is a direct input from 2D flow simulations in the set of conditions C. In turn, the flow model takes the $n_e(r)$ and $P_{abs}(r)$ profiles as input. This has been done firstly using the assumptions from eq. 8 and 9, *i.e.*, $\Lambda_{P_{abs}} = \Lambda_{n_e} = \Lambda_{777}$. In this work, the $n_e(r)$ and $P_{abs}(r)$ profiles are corrected for the 7 cases of the set of conditions C, using the ratios found here. Indeed, these profiles are taken with approximately 1.6 times higher radial and axial FWHM, and used as input in the model described in *Wolf et al.* [2020a]. As n_e is conserved line-integrated and P_{abs} is conserved volume integrated, their peaks are, respectively, around 1.6 and 4 times lower. Different simulation results are obtained with these inputs, with respect to the initial ones using the assumptions from eq. 8 and 9. To show the resulting difference, the initial and corrected radial profiles of T_g and x_O at the axial position of highest T_g are represented in figure 13 for 121 mbar and 296 mbar. Besides the importance of x_O and T_g for the study of spatial profiles of discharge parameters, we have seen in figures 2 and 3 that T_g and x_O are correlated with the production of CO, the dissociation product that these reactors are aimed at producing.
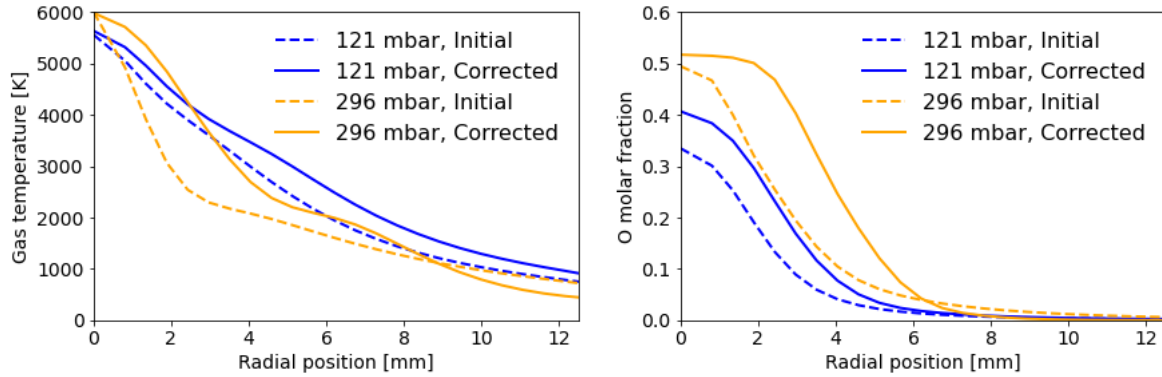
Figure 13. Radial profiles of flow model results, using the initial assumptions on $n_e(r)$ and $P_{abs}(r)$ ($\Lambda_{P_{abs}} = \Lambda_{n_e} = \Lambda 777$), and the corrected $n_e(r)$ and $P_{abs}(r)$ profiles with $\Lambda_{P_{abs}} \sim \Lambda_{n_e} \sim 1.6 \times \Lambda 777$. Gas temperature is represented on the left and O molar fraction on the right.

In the flow model in *Wolf et al.* [2020a], the peak gas temperature is set to the one measured in Doppler broadening measurements [*Wolf et al.*, 2019]. As such, the broader profile of P_{abs} leads to the same peak temperature but a slightly broader high-temperature profile, as shown in figure 13. Although apparently small, this broadening increases thermally-driven dissociation in the plasma and hence produces higher and more extended profiles of O and CO molar fractions, as shown on the right side of the same figure. This effect is reinforced by the broadening of the $n_e(r)$ profile driving electron-impact dissociation reactions.

Nbr.	Hypothesis	Verification
1	$I_{777} \simeq \tau_{\text{rad}}^{-1} \dfrac{n_e \ n_{O(2p^4 \ ^3P)} \ k_{\text{exc}}(T_e)}{\tau_{\text{rad}}^{-1} + n_g \ k_Q}$	Approximately valid
2	$I_{777} \propto n_e \ x_O \ k_{\text{exc}}(T_e)$	$I_{777} \propto \tau_{\text{rad}}^{-1} \ n_e \ x_O \ k_{\text{eff}}(T_e)$
3	E/n_g and k_{exc} radially homogeneous	E/n_g concave and $k_{\text{exc}} \propto n_e$
4	$I_{777} \propto n_e^s, 1 \leq s \leq 2$	$I_{777} \propto n_e^s, 1.82 \leq s \leq 2.94, s \sim 2.5$
5	x_O radially homogeneous	Measured x_O concave or homogeneous
6	$I_{777} \propto n_e \propto P_{\text{abs}}$	$I_{777} \propto P_{\text{abs}}^{s_p}, 1.22 \leq s_p \leq 2.50, s_p \sim 2.5$

Table 5. Summary of the hypotheses listed in section 2.1 and of the results of the numerical and experimental verifications performed in this work.

The changes in temperature and composition have an influence on the study of spatial profiles undergone in the current work, and the two models (flow and plasma) are therefore interdependent. The plasma simulations are run for the corrected cases of the set of conditions C to verify the consistency of our results. For $p < 150$ mbar, the dependence between I_{777}, n_e and P_{abs} is very similar with or without this correction, as the corrected x_O has higher values but a similar radial profile as in the initial assumption. However, for highly-contracted conditions with $p > 150$ mbar, the correction leads to a more flat profile of $x_O(r)$, similar to the one presented in figure 3, and therefore to a dependence between the studied parameters that is closer to that of condition B. As such, in those cases the interdependence between the inputs of the two models is not fully consistent. We can only conclude that the values of the ratios $\Lambda_{n_e}/\Lambda_{777}$ and $\Lambda_{P_{\text{abs}}}/\Lambda_{777}$ stand between those of condition B, respectively 1.32 and 1.08, and those of figure 12, both close to 1.6. Although allowing for the study of a wider parameter range, the interdependence between the two models presents some limitations with respect to using the plasma model with experimentally measured input. Those limitations can be overcome through the development of a self-consistent model simulating flow, temperature, composition and plasma parameters.

Gathering the results of conditions A, B and C, we can say that the proportionality between n_e, P_{abs} and I_{777} can be described as $I_{777} \propto n_e^s, 1.82 \leq s \leq 2.94$ and $I_{777} \propto P_{\text{abs}}^{s_p}, 1.22 \leq s_p \leq 2.50$. The disparity between these proportionality parameters shows that the spatial resolution of discharge parameters from emission intensity is rather complex and dependent on particular conditions. As such, spatially-resolved measurements and simulations are two essential and complementary tools to accurately describe the spatial profiles of discharge parameters in contracted plasmas. Moreover, we should notice that, despite the complexity, Λ_{n_e} and $\Lambda_{P_{\text{abs}}}$ are around 1.6 times higher than Λ_{777} for $p < 150$ mbar and the values of the proportionality parameters s and s_p are close to 2.5. Hence, these values can be assumed for MW CO_2 contracted plasmas that are not fully contracted, *i.e.*, whose contraction regime is not H-mode according to the characterisation in *Wolf et al.* [2020b]. Based on this modelling study, our evaluation of the hypotheses listed in section 2.1 is summarised in table 5.

Resolving discharge parameters from atomic oxygen emission 　　　　　　34

4.4. Discussion on implications of the correction of radial profiles of plasma parameters

The contracted MW discharges for CO_2 conversion have been studied in detail in the experimental works in *Wolf et al.* [2019] and *Wolf et al.* [2020b]. In *Wolf et al.* [2019], the electron density in the MW CO_2 conversion discharge has been measured line-integrated, and its peak n_{e0} has been taken from $n_{e\Lambda}$ (eq. 6) assuming $s = 1$, *i.e.* that $\Lambda_{n_e} = \Lambda_{777}$. This measurement, along with that of T_g in the plasma core through Doppler broadening, has revealed an ionisation degree in the core (n_{e0}/n_{g0}) of the order of 10^{-5} in L-mode conditions and rising to 10^{-4} in H-mode. Moreover, it has been established in *Wolf et al.* [2019] that the plasma radius $\Lambda_{n_e}/2$ is of the same order of the skin-depth of MW absorption and that n_{e0}/n_{g0} is approximately inversely proportional to the square of the plasma diameter: $n_{e0}/n_{g0} \propto \Lambda_{n_e}^{-2}$. These assertions characterise discharge contracted modes and have been completed by the study in *Wolf et al.* [2020b], where the mechanism of thermo-chemical instability has been proposed to explain the relationship between mode transition and T_g. The present study further supplements this body of work, finding that, for the conditions of relevance, $\Lambda_{n_e} \simeq 1.6 \times \Lambda_{777}$ and thus that n_{e0} has been previously overestimated by approximately a factor 1.6. This finding allows to correct the calculations from previous works and should be considered in studies of discharge contraction, a phenomenon that depends on electron-impact ionisation and recombination rates. However, the correction does not affect the conclusions from *Wolf et al.* [2019] and *Wolf et al.* [2020b] concerning mode transition and ionisation degree.

The study of these contracted discharges has been complemented by the numerical investigations in *Groen et al.* [2019] and *Viegas et al.* [2020]. As mentioned previously, in *Groen et al.* [2019] a 3D electromagnetic model has simulated the spatial distributions of electric field in these plasmas, given an input profile of n_e. The assumption of $s = 1$ has been used to determine that profile in both the radial and axial directions. For the case of a low-confinement discharge at 100 mbar with a maximum temperature around 4000 K, a $n_e(r)$ profile with similar FWHM as the corrected Λ_{n_e} in condition A in this work ($\sim$ 10 mm) but 6 times lower peak, has been considered in *Groen et al.* [2019]. The resulting radial profiles of E and E/n_g are rather flat for $r < 4$ mm, with values almost twice as much as those reported for condition A in this work (figure 8), and have a convex shape radially outwards. Conversely, in this work, E/n_g has a concave radial profile and E is approximately flat up to $r = 10$ mm. We should notice that different assumptions have been taken on the T_g and n_e profiles and that the method to simulate the electric field is significantly different. While in the plasma reaction-diffusion model of this work $E/n_g(r)$ is found by matching the input $n_e(r)$, in *Groen et al.* [2019] E has been found in the whole domain for a given n_e profile by matching the impedance of the plasma with that of the incoming MW field. The model in *Groen et al.* [2019] finds E by solving Maxwell's equations and by assuming power deposition through Ohmic heating and a homogeneous electron-neutral collision frequency. The finding from this work that $\Lambda_{n_e} \simeq 1.6 \times \Lambda_{777}$ means that the profile of n_e should be even broader than that used in *Groen et al.* [2019]. The adoption of a broader profile of n_e in the model of *Groen et al.*

[2019] would arguably lead to a broader profile of E, *i.e.* a profile of E rather flat along a region larger than 4 mm radius. Furthermore, with higher values of n_{e}, it is predicted that lower values of E would be required to maximise the power transfer to the plasma. Finally, for radial positions beyond the plasma, the different ways of calculating the electric field in the different models determine that $E(r)$ increases with r in *Groen et al.* [2019] and decreases with r in this work, which should not be directly compared. Taking these features into account, the profiles of $E(r)$ and $E/n_{\mathrm{g}}(r)$ simulated with the models in *Groen et al.* [2019] and in this work are expected to be coherent with each other.

The numerical study in *Viegas et al.* [2020] using a zero-dimensional model has also taken n_{e0} as input under the assumption of $s = 1$, mostly in the plasma conditions described in this work as set of conditions C. However, the model in *Viegas et al.* [2020] has not directly used any assumption on $\Lambda_{n_{\mathrm{e}}}$. We should notice that the correction associated to the interferometry measurements described in section 2.2 would lead most of the n_{e0} values used in *Viegas et al.* [2020] (those in hybrid regime and in H-mode) to increase by a factor of approximately 1.5. We have also seen in figure 12 that n_{e0} should be divided by about 1.6, due to the phenomenon of optical contraction. As a result, the two corrections would lead the input values of n_{e0} used in *Viegas et al.* [2020] to stay approximately the same. As such, no significant changes are expected in the simulation results and in the conclusions in that paper. Indeed, despite the different models, the values of peak power density simulated in that work are very similar to the corrected P_{abs0} obtained for the set of conditions C in this work, since the biggest contribution to the calculation of P_{abs0} is the local collisional term in eq. 18. However, in *Viegas et al.* [2020], the simulated P_{abs0} has been compared to the experimentally-estimated one (see figure 3 in *Viegas et al.* [2020]). Experimentally, P_{abs0} in the centre of the plasma has been obtained, as described in *Wolf et al.* [2020b], by normalisation of the power density profile to the total power input. This profile has been assumed the same as the one of emission intensity. If, by following the results of this work, 1.6 times higher diameter and length were assumed for the Gaussian profile of P_{abs}, we could expect P_{abs0} to be $1.6^3 \simeq 4$ times lower. This is a very important difference that appears as the result of the current study. Concerning the comparison of numerical and experimental P_{abs0} in figure 3 of *Viegas et al.* [2020], this correction would explain the discrepancies observed and would lead to a significantly better agreement for pressures below 200 mbar, which increases our confidence in the validity of that model.

The two-dimensional model in *Wolf et al.* [2020a], that predicts reactor performances and the mechanisms to obtain them, is also dependent on the spatial profiles of n_{e} and P_{abs}, as explained in the previous section. As shown in figure 13, the broadening of these profiles leads to a broader high-temperature profile and increased dissociation in the plasma region. However, a more extended temperature profile also leads to slower cooling downstream and thus a broader recombination region. The result of these two effects is higher conversion and energy efficiencies of the simulated reactor at pressures below 140 mbar but lower performances at higher pressures. The broadening of the P_{abs} profile in the flow model and the decrease of its peak also has an influence

Resolving discharge parameters from atomic oxygen emission 36

on the peak of the turbulent viscosity ($\nu_{\mathrm{T,peak}}$ in eq. 16), that is adjusted to match the peak gas temperature with the one measured in Doppler broadening measurements [*Wolf et al.*, 2019]. Indeed, lower $\nu_{\mathrm{T,peak}}$ is obtained, which leads to less gas mixing in the simulated domain. However, the broadening of the high-temperature profile allows for dissociation further from the plasma core and thus the negative effect for dissociation of lower gas mixing becomes negligible. The energy efficiencies simulated with the flow model before and after the correction of the spatial profiles are compared in figure 14 for the 7 cases of the set of conditions C. The increase of these efficiencies at lower pressures improves the agreement of the flow simulations with experimental measurements (figure 6 in *Wolf et al.* [2020a]), as the broader spatial profiles of P_{abs} and T_{g} explain the high experimental conversions at low pressure. It is shown that the accurate determination of spatial profiles of discharge parameters should be taken into account when analysing reactor performances. However, for pressures above 140 mbar, the agreement between the flow simulations and the measurements does not improve with the correction. This reinforces the statement in *Wolf et al.* [2020a] according to which the energy efficiency at higher pressures depends on the recombination of CO downstream from the plasma, and thus on the neutral chemistry for temperatures below 2000 K.
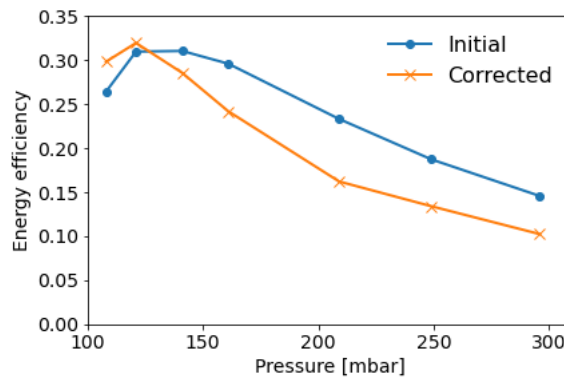
Figure 14. Energy efficiencies as function of pressure, simulated with the flow model in *Wolf et al.* [2020a], using the initial assumptions on $n_{\mathrm{e}}(r)$ and $P_{\mathrm{abs}}(r)$ ($\Lambda_{\mathrm{P_{abs}}} = \Lambda_{\mathrm{n_e}} = \Lambda 777$), and the corrected $n_{\mathrm{e}}(r)$ and $P_{\mathrm{abs}}(r)$ profiles with $\Lambda_{\mathrm{P_{abs}}} \sim \Lambda_{\mathrm{n_e}} \sim 1.6 \times \Lambda 777$. Results obtained for the set of conditions C.

Although in this section we have focused on the implications of spatially-resolved plasma parameters for the study of MW contracted discharges for CO_2 conversion, we expect the methods proposed in this work to be relevant for research on other discharges. Firstly, because we have shown that the phenomenon of optical contraction is present not only in atomic plasmas [*Golubovskii et al.*, 2011, 2020], but also in a molecular gas like CO_2. More generally, we can say that, as spatially-resolved parameters are often difficult to measure, spontaneous optical emission, a natural phenomenon in non-equilibrium plasmas, can provide valuable insight into the spatial distribution of key plasma parameters when interpreted using spatially resolved CRMs. This is particularly the case in plasma sources where the spatial distribution of optical emission is clearly

1
2
3
4
5
6
7
8
9
10
11
12
13
14
15
16
17
18
19
20
21
22
23
24
25
26
27
28
29
30
31
32
33
34
35
36
37
38
39
40
41
42
43
44
45
46
47
48
49
50
51
52
53
54
55
56
57
58
59
60

Resolving discharge parameters from atomic oxygen emission 37

measurable, such as in steady-state DC, RF and MW discharges in cylindrical containers with radii of a few mm or a few cm. Another requirement for the application of the proposed approach is the previous knowledge of line-averaged or volume-averaged values of electron density or electric field or power density, allowing to take assumptions on their spatial profiles and then correcting them. Other experimental measurements are not required for the application of the methods proposed, although they may be useful as additional model inputs to guarantee that simulations and experiments assess the same conditions. Following the approach we have employed in this work allows to find spatial profiles of different plasma parameters that are important for both understanding and application of discharges.

Resolving discharge parameters from atomic oxygen emission 38

5. Conclusions

In the present study, a method has been presented to obtain spatially-resolved discharge parameters from emission intensity measurements. Contracted MW discharges for CO_2 conversion at intermediate to high pressures (100 to 300 mbar) have been addressed, where spatial distributions of the Abel-inverted intensity of the 777 nm line emission $(O(3p\ ^5P) \rightarrow O(3s\ ^5S^0))$, I_{777}, have been measured. Previous experimental studies on these discharges have relied on unverified assumptions on the spatial profiles of discharge parameters, such as electron density (n_e), power density (P_{abs}) and reduced electric field (E/n_g). These profiles have been based on the Gaussian spatial distribution of I_{777}. In this paper, a 1D-radial reaction-diffusion plasma model, including a CRM of atomic oxygen, has been developed and used to resolve discharge parameters in space, by matching the measured I_{777} profiles. It is the first time that such a model has been developed in the context of reactive CO_2 mixtures and used in different conditions of low-confinement and high-confinement discharges. The simulations have allowed us to verify that the experimentally-assumed profile of n_e is not fully consistent with the measurements of the FWHM of I_{777}. Then, they have been used to derive more accurate spatial profiles of n_e, P_{abs} and E/n_g, that have been shown to be consistent with the measurements of I_{777}. Therefore, we have proposed to use this model to obtain accurate radially-resolved discharge parameters from simulations using experimental input.

The numerically-obtained radial profiles of n_e at intermediate to high pressures follow a Gaussian curve with a lower peak than initially assumed and a higher FWHM than the experimentally-observed I_{777}. This phenomenon has been called optical contraction when first reported for atomic plasmas, and has been observed here for the first time in CO_2 MW discharges. According to the simulation results, the optical contraction is mostly justified by a concave profile of E/n_g, resulting from the self-reinforcing cycle of electron-driven collisionality and gas heating in contracted discharges. This leads to an approximately linear relationship between n_e and the electron-impact excitation coefficient of $O(3p\ ^5P)$, the upper state of the 777 nm transition. The optical contraction is also promoted by the concave radial profile of the molar fraction of atomic oxygen in the CO_2 conversion plasma, measured through Raman scattering, that in low-confinement conditions is almost linearly proportional to n_e. The numerically-obtained radial profile of P_{abs} is close to the one of n_e. The relationships between P_{abs}, n_e and I_{777} have been shown to be complex and dependent on particular conditions. However, we can generally say that for pressures below 150 mbar the FWHM of P_{abs} and n_e are around 1.6 times higher than that of I_{777}. That implies that the peaks of n_e and P_{abs} are, respectively, around 1.6 and $1.6^3 \sim 4$ times lower than previously considered.

Finally, the implications of the proposed corrections to the spatial profiles of discharge parameters on the study of contracted microwave discharges for CO_2 conversion have been demonstrated and discussed. The corrections have an impact on our perception of the discharge diameter and of the electric field and power density

distributions in the plasma, as well as on our understanding of the main mechanisms determining reactor performances. Indeed, the broader profile of P_{abs} than initially supposed explains the high conversion rates measured for pressures below 140 mbar. Moreover, we have proposed that the procedure developed in this work to determine spatial profiles of discharge parameters can be easily used for the study of plasmas with different configurations and different gases. It has been demonstrated that by combining spatially-resolved numerical simulations with experimental measurements, including measurements of radiative emission intensity, other plasma parameters, such as n_{e}, P_{abs} and E/n_{g}, can be retrieved with spatial resolution and replace commonly-used assumptions.

Resolving discharge parameters from atomic oxygen emission   40

Acknowledgments

REFERENCES   41

References

Alves, L., P. Coche, M. A. Ridenti, and V. Guerra (2016), Electron scattering cross sections for the modelling of oxygen-containing plasmas, *Eur. Phys. J. D*, *70*(124), www.lxcat.net/IST-Lisbon, retrieved on January 30, 2020.

Alves, L. L., A. Bogaerts, V. Guerra, and M. M. Turner (2018), Foundations of modelling of nonequilibrium low-temperature plasmas, *Plasma Sources Sci. Technol.*, *27*(023002).

Annušová, A., D. Marinov, J. P. Booth, N. Sirse, M. L. da Silva, B. Lopez, and V. Guerra (2018), Kinetics of highly vibrationally excited $O_2(X)$ molecules in inductively-coupled oxygen plasmas, *Plasma Sources Sci. Technol.*, *27*(045006).

Baeva, M., F. Hempel, H. Baier, T. Trautvetter, R. Foest, and D. Loffhagen (2018), Two- and three-dimensional simulation analysis of microwave excited plasma for deposition applications: operation with argon at atmospheric pressure, *J. Phys. D: Appl. Phys.*, *51*(385202).

Barklem, P. S. (2007), Electron-impact excitation of neutral oxygen, *Astron. Astrophys.*, *462*, 781–788.

Bongers, W., H. Bouwmeester, B. Wolf, F. Peeters, S. Welzel, D. C. M. van den Bekerom, N. den Harder, A. Goede, M. Graswinckel, P. W. Groen, J. Kopecki, M. Leins, G. van Rooij, A. Schulz, M. Walker, and R. van de Sanden (2017), Plasma-driven dissociation of CO_2 for fuel synthesis, *Plasma Process. Polym.*, *14*(e1600126).

Butylkin, Y. P., V. K. Zhivotov, E. G. Krasheninnikov, M. F. Krotov, V. D. Rusanov, Y. V. Tarasov, and A. A. Fridman (1981), Dissociation of CO_2 by a plasma-chemical process in a nonequilibrium microwave discharge, *Sov. Phys. Tech. Phys.*, *26*, 555–558.

Capitelli, M., D. Bruno, and A. Laricchiuta (2013), *Fundamental aspects of plasma chemical physics: Transport*, Springer Science & Business Media.

Capitelli, M., R. Celiberto, G. Colonna, F. Esposito, C. Gorse, K. Hassouni, A. Laricchiuta, and S. Longo (2015), *Fundamental aspects of plasma chemical physics: Kinetics*, vol. 85, Springer Science & Business Media.

Caplinger, J. E., and G. P. Perram (2020), The importance of cascade emission and metastable excitation in modeling strong atomic oxygen lines in laboratory plasmas, *Plasma Sources Sci. Technol.*, *29*(015011).

Carbone, E. A. D., S. Hubner, J. M. Palomares, and J. J. A. M. van der Mullen (2012), The radial contraction of argon microwave plasmas studied by Thomson scattering, *J. Phys. D: Appl. Phys.*, *45*(345203).

Dagdigian, P. J., B. E. Forch, and A. W. Miziolek (1988), Collisional transfer between and quenching of the $3p^3P$ and ^5P states of the oxygen atom, *Chem. Phys. Lett.*, *148*(4), 299–308.

den Harder, N., D. C. M. van den Bekerom, R. S. Al, M. F. Graswinckel, J. M. Palomares, F. J. J. Peeters, S. Ponduri, T. Minea, W. A. Bongers, M. C. M. van de

REFERENCES   42

Sanden, and G. J. van Rooij (2017), Homogeneous CO_2 conversion by microwave plasma: Wave propagation and diagnostics, *Plasma Process. Polym.*, *14* (e1600120).

D'Isa, F. A., E. A. D. Carbone, A. Hecimovic, and U. Fantz (2020), Performance analysis of a 2.45 GHz microwave plasma torch for CO_2 decomposition in gas swirl configuration, *Plasma Sources Sci. Technol.*, *29* (105009).

Durandet, A., Y. Arnal, J. Margot-Chaker, and M. Moisan (1989), Investigation of a plasma source sustained by an electromagnetic surface wave at 2.45 GHz under free-fall regime, *J. Phys. D: Appl. Phys.*, *22* (1288).

Dyatko, N. A., Y. Z. Ionikh, I. V. Kochetov, D. L. Marinov, A. V. Meshchanov, A. P. Napartovich, F. B. Petrov, and S. A. Starostin (2008), Experimental and theoretical study of the transition between diffuse and contracted forms of the glow discharge in argon, *J. Phys. D: Appl. Phys.*, *41* (055204).

Eliasson, B., and U. Kogelschatz (1986), Electron impact dissociation in oxygen, *J. Phys. B: At. Mol. Phys.*, *19*, 1241–1247.

Erdman, P. W., and E. C. Zipf (1987), Excitation of the OI($3s^5S^0$ - $3p^5P$; λ 7774 Å) multiplet by electron impact on O_2, *J. Chem. Phys.*, *87* (4540).

Fiebrandt, M., B. Hillebrand, S. Spiekermeier, N. Bibinov, M. Boke, and P. Awakowicz (2017), Measurement of Ar resonance and metastable level number densities in argon containing plasmas, *J. Phys. D: Appl. Phys.*, *50* (355202).

Fiebrandt, M., N. Bibinov, and P. Awakowicz (2020), Determination of atomic oxygen state densities in a double inductively coupled plasma using optical emission and absorption spectroscopy and probe measurements, *Plasma Sources Sci. Technol.*, *29* (045018).

Fleisch, T., Y. Kabouzi, M. Moisan, J. Pollak, E. C. Martinez, H. Nowakowska, and Z. Zakrzewski (2007), Designing an efficient microwave-plasma source, independent of operating conditions, at atmospheric pressure, *Plasma Sources Sci. Technol.*, *16*, 173–182.

Fridman, A. (2008), *Plasma chemistry*, Cambridge University Press.

Fridman, A., and L. A. Kennedy (2004), *Plasma physics and engineering*, Taylor and Francis Routledge.

Georgieva, V., A. Berthelot, T. Silva, S. Kolev, W. Graef, N. Britun, G. Chen, J. van der Mullen, T. Godfroid, D. Mihailova, J. van Dijk, R. Snyders, A. Bogaerts, and M.-P. Delplancke-Ogletree (2017), Understanding microwave surface-wave sustained plasmas at intermediate pressure by 2D modeling and experiments, *Plasma Process. Polym.*, *14* (1600185).

Giovangigli, V. (1990), Mass conservation and singular multicomponent diffusion algorithms, *Impact of computing in science and engineering*, *2*, 73–97.

Goede, A. P. H., W. A. Bongers, M. F. Graswinckel, M. C. M. van de Sanden, M. Leins, J. Kopecki, A. Schulz, and M. Walker (2014), Production of solar fuels by CO_2 plasmolysis, *EPJ Web of Conferences*, *79* (01005).

REFERENCES 43

Golubovskii, Y. B., V. Nekuchaev, S. Gorchakov, and D. Uhrlandt (2011), Contraction of the positive column of discharges in noble gases, *Plasma Sources Sci. Technol.*, *20*(053002).

Golubovskii, Y. B., D. Kalanov, and V. Maiorov (2017), Radial structure of the constricted positive column: Modeling and experiment, *Phys. Rev. E*, *96*(023206).

Golubovskii, Y. B., A. V. Siasko, and V. Nekuchaev (2020), Peculiarities of glow discharge constriction in helium, *Plasma Sources Sci. Technol.*, *29*(065020).

Gordiets, B. F., C. M. Ferreira, V. L. Guerra, J. M. A. H. Loureiro, J. Nahorny, D. Pagnon, M. Touzeau, and M. Vialle (1995), Kinetic model of a low-pressure N_2-O_2 flowing glow discharge, *IEEE Transactions on Plasma Science*, *23*(4), 750–768.

Gregório, J., C. Boisse-Laporte, and L. L. Alves (2010), Fluid modeling of a microwave micro-plasma at atmospheric pressure, *Eur. Phys. J. Appl. Phys.*, *49*(13102).

Gregório, J., P. Leprince, C. Boisse-Laporte, and L. L. Alves (2012), Self-consistent modelling of atmospheric micro-plasmas produced by a microwave source, *Plasma Sources Sci. Technol.*, *21*(015013).

Groen, P. W. C., A. J. Wolf, T. W. H. Righart, M. C. M. van de Sanden, F. J. J. Peeters, and W. A. Bongers (2019), Numerical model for the determination of the reduced electric field in a CO_2 microwave plasma derived by the principle of impedance matching, *Plasma Sources Sci. Technol.*, *28*(075016).

Grofulović, M., L. L. Alves, and V. Guerra (2016), Electron-neutral scattering cross sections for CO_2: a complete and consistent set and an assessment of dissociation, *J. Phys. D: Appl. Phys.*, *49*, 395,207.

Guerra, V., T. Silva, P. Ogloblina, M. Grofulovíc, L. Terraz, M. L. da Silva, C. D. Pintassilgo, L. L. Alves, and O. Guaitella (2017), The case for in situ resource utilisation for oxygen production on Mars by non-equilibrium plasmas, *Plasma Sources Sci. Technol.*, *26*, 11LT01.

Hirschfelder, J. O., and C. F. Curtiss (1949), Flame propagation in explosive gas mixtures, *In third symposium on combustion, flame and explosion phenomena*, pp. 121–127.

Ikegami, H. (1968), Scattering of microwaves from a plasma column in rectangular waveguide, *Jpn. J. Appl. Phys.*, *7*, 634–655.

Itikawa, Y. (2009), Cross sections for electron collisions with oxygen molecules, *J. Phys. Chem. Ref. Data*, *38*(1).

Jimenez-Diaz, M., E. A. D. Carbone, J. van Dijk, and J. J. A. M. van der Mullen (2012), A two-dimensional Plasimo multiphysics model for the plasma–electromagnetic interaction in surface wave discharges: the surfatron source, *J. Phys. D: Appl. Phys.*, *45*(335204).

Kabouzi, Y., D. B. Graves, E. C. Martinez, and M. Moisan (2007), Modeling of atmospheric-pressure plasma columns sustained by surface waves, *Phys. Rev. E*, *75*(016402).

REFERENCES   44

Kanik, I., C. Noren, O. P. Makarov, P. Vattipalle, J. M. Ajello, and D. E. Shemansky (2003), Electron impact dissociative excitation of O_2: 2. Absolute emission cross sections of the OI(130.4 nm) and OI(135.6 nm) lines, *J. Geophys. Res.*, *108*(5126).

Koelman, P., S. Heijkers, S. T. Mousavi, W. Graef, D. Mihailova, T. Kozák, A. Bogaerts, and J. van Dijk (2017), A comprehensive model for the splitting of CO_2 in non-equilibrium plasmas, *Plasma Process. Polym.*, *14*(1600155).

Kossyi, A., A. Y. Kostinsky, A. A. Matveyev, and V. P. Silakov (1992), Kinetic scheme of the non-equilibrium discharge in nitrogen-oxygen mixtures, *Plasma Sources Sci. Technol.*, *1*, 207–220.

Kozák, T., and A. Bogaerts (2014), Splitting of CO_2 by vibrational excitation in non-equilibrium plasmas: a reaction kinetics model, *Plasma Sources Sci. Technol.*, *23*(045004).

Kramida, A., Y. Ralchenko, J. Reader, and N. A. Team (2020), NIST Standard Reference Database 78 - Atomic Spectra Database (ver. 5.8), National Institute of Standards and Technology, Gaithersburg, https://dx.doi.org/10.18434/T4W30F.

Laher, R. R., and F. R. Gilmore (1990), Updated excitation and ionization cross sections for electron impact on atomic oxygen, *J. Phys. Chem. Ref. Data*, *19*(277).

Laricchiuta, A., D. Bruno, M. Capitelli, C. Catalfamo, R. Celiberto, G. Colonna, P. Diomede, D. Giordano, C. Gorse, S. Longo, D. Pagano, and F. Pirani (2009), High temperature Mars atmosphere. Part I: transport cross sections, *Eur. Phys. J. D*, *54*, 607–612.

Lawrence, G. M. (1970), Dissociative excitation of some oxygen-containing molecules: Lifetimes and electron-impact cross sections, *Phys. Rev. A*, *2*, 387–407.

Lieberman, M. A., and A. J. Lichtenberg (2005), *Principles of plasma discharges and materials processing*, Wiley-Interscience.

Martinez, E. C., Y. Kabouzi, K. Makasheva, and M. Moisan (2004), Modeling of microwave-sustained plasmas at atmospheric pressure with application to discharge contraction, *Phys. Rev. E*, *70*(066405).

McConkey, J. W., C. P. Malonea, P. V. Johnson, C. Winstead, V. McKoy, and I. Kanik (2008), Electron impact dissociation of oxygen-containing molecules - a critical review, *Physics Reports*, *466*, 1–103.

Mewe, R. (1967), Relative intensity of helium spectral lines as a function of electron temperature and density, *Brit. J. Appl. Phys.*, *18*, 107–118.

Moisan, M., and J. Pelletier (2012), *Physics of collisional plasmas: Introduction to high-frequency discharges*, Springer.

Mori, T., K. Kanou, K. Mizuta, T. Kuramasu, Y. Ishikawa, and S. Arai (1992), Reactions of highly excited oxygen atoms $O(2p^33s,^5S)$ with simple gas molecules, *J. Chem. Phys.*, *97*(9094).

REFERENCES 45

Morillo-Candas, A. S., C. Drag, J.-P. Booth, T. C. Dias, V. Guerra, and O. Guaitella (2019), Oxygen atom kinetics in CO_2 plasmas ignited in a DC glow discharge, *Plasma Sources Sci. Technol.*, *28*(075010).

Mousavi, S. T., E. Carbone, A. Wolf, W. Bongers, and J. van Dijk (2021), Two-temperature balance equations implementation, numerical validation and application to H_2O-He microwave induced plasmas, *In press.*

Niemi, K., V. S. von der Gathen, and H. F. Dobele (2001), Absolute calibration of atomic density measurements by laser-induced fluorescence spectroscopy with two-photon excitation, *J. Phys. D: Appl. Phys.*, *34*, 2330–2335.

Parker, J. V. (1963), Collisionless plasma sheath in cylindrical geometry, *Phys. Fluids*, *6*, 1657–8.

Patankar, S. V. (1980), *Numerical heat transfer and fluid flow*, Taylor & Francis group, LLC.

Petrov, G. M., and C. M. Ferreira (1999), Numerical modeling of the constriction of the dc positive column in rare gases, *Phys. Rev. E*, *59*, 3571–3582.

Pietanza, L. D., G. Colonna, and M. Capitelli (2020), Kinetics versus thermodynamics on CO_2 dissociation in high temperature microwave discharges, *Plasma Sources Sci. Technol.*, *29*(035022).

Ridenti, M. A., J. D. Amorim, A. D. Pino, V. Guerra, and G. Petrov (2018), Causes of plasma column contraction in surface-wave-driven discharges in argon at atmospheric pressure, *Phys. Rev. E*, *97*(013201).

Santos, M., C. Noel, T. Belmonte, and L. L. Alves (2014), Microwave capillary plasmas in helium at atmospheric pressure, *J. Phys. D: Appl. Phys.*, *47*(265201).

Schaefer, G., and P. Hui (1990), The Monte Carlo flux method, *J. Comput. Phys.*, *89*, 1–30.

Schottky, W. (1924), Diffusionstheorie der positiven säule, *Phys. Zeits.*, *25*(342).

Shneider, M. N., M. S. Mokrov, and G. M. Milikh (2014), Dynamic contraction of the positive column of a self-sustained glow discharge in air flow, *Phys. Plasmas*, *21*(032122).

Silva, A. F., A. S. Morillo-Candás, A. T. del Caz, L. L. Alves, O. Guaitella, and V. Guerra (2020), A reaction mechanism for vibrationally-cold low-pressure CO_2 plasmas, *Plasma Sources Sci. Technol.*, *29*(125020).

Smith, G. P., D. M. Golden, M. Frenklach, N. W. Moriarty, B. Eiteneer, M. Goldenberg, C. T. Bowman, R. K. Hanson, S. Song, W. C. G. Jr., V. V. Lissianski, and Z. Qin (2018), GRI-MECH 3.0, http://combustion.berkeley.edu/gri-mech/version30/text30.html.

Snoeckx, R., and A. Bogaerts (2017), Plasma technology - a novel solution for CO_2 conversion?, *Chem. Soc. Rev.*, *46*, 5805–5863.

REFERENCES 46

Stancu, G. D., O. Leroy, P. Coche, K. Gadonna, V. Guerra, T. Minea, and L. L. Alves (2016), Microwave air plasmas in capillaries at low pressure II. Experimental investigation, *J. Phys. D: Appl. Phys.*, *49*(435202).

Sushkov, V. P., H. T. Do, and R. Hippler (2013), Application of the escape factor method for determination of excited states densities in a low-pressure argon radio-frequency discharge, *Contrib. Plasma Phys.*, *53*, 549–559.

Synek, P., A. Obrusník, S. Hübner, S. Nijdam, and L. Zajíčková (2015), On the interplay of gas dynamics and the electromagnetic field in an atmospheric Ar/H_2 microwave plasma torch, *Plasma Sources Sci. Technol.*, *24*(025030).

van de Steeg, A. W., T. Butterworth, D. C. M. van den Bekerom, A. F. Silva, M. C. M. van de Sanden, and G. J. van Rooij (2020), Plasma activation of N_2, CH_4 and CO_2: an assessment of the vibrational non-equilibrium time window, *Plasma Sources Sci. Technol.*, *29*(115001).

van de Steeg, A. W., L. Vialetto, A. F. Silva, F. J. J. Peeters, D. C. M. van den Bekerom, N. Gatti, P. Diomede, M. C. M. van de Sanden, and G. J. van Rooij (2021), Revisiting spontaneous Raman scattering for direct oxygen atom quantification, *Optics Letters*, *46*, 2172–2175.

van den Bekerom, D. C. M., J. M. P. Linares, T. Verreycken, E. M. van Veldhuizen, S. Nijdam, G. Berden, W. A. Bongers, M. C. M. van de Sanden, and G. J. van Rooij (2019), The importance of thermal dissociation in CO_2 microwave discharges investigated by power pulsing and rotational Raman scattering, *Plasma Sources Sci. Technol.*, *28*(055015).

van den Bekerom, D. C. M., A. van de Steeg, M. C. M. van de Sanden, and G. J. van Rooij (2020), Mode resolved heating dynamics in pulsed microwave CO_2 plasma from laser Raman scattering, *J. Phys. D: Appl. Phys.*, *53*(054002).

van Gessel, A. F. H., E. A. D. Carbone, P. J. Bruggeman, and J. J. A. M. van der Mullen (2012), Laser scattering on an atmospheric pressure plasma jet: disentangling Rayleigh, Raman and Thomson scattering, *Plasma Sources Sci. Technol.*, *21*(015003).

van Rooij, G. J., D. C. M. van den Bekerom, N. den Harder, T. Minea, G. Berden, W. A. Bongers, R. Engeln, M. F. Graswinckel, E. Zoethout, and M. C. M. van de Sanden (2015), Taming microwave plasma to beat thermodynamics in CO_2 dissociation, *Faraday Discuss.*, *183*, 233–248.

Vermeiren, V., and A. Bogaerts (2020), Plasma-based CO_2 conversion: To quench or not to quench?, *J. Phys. Chem. C*, *124*, 18,401–18,415.

Vialetto, L., S. Longo, and P. Diomede (2019), Benchmark calculations for electron velocity distribution function obtained with Monte Carlo Flux simulations, *Plasma Sources Sci. Technol.*, *28*(115015).

Vialetto, L., P. Viegas, S. Longo, and P. Diomede (2020), Benchmarking of Monte Carlo flux simulations of electrons in CO_2, *Plasma Sources Sci. Technol.*, *29*(115006).

REFERENCES   47

Viegas, P., L. Vialetto, A. J. Wolf, F. J. J. Peeters, P. W. C. Groen, T. W. H. Righart, W. A. Bongers, M. C. M. van de Sanden, and P. Diomede (2020), Insight into contraction dynamics of microwave plasmas for CO_2 conversion from plasma chemistry modelling, *Plasma Sources Sci. Technol.*, *29*(105014).

Wolf, A. J., T. W. H. Righart, F. J. J. Peeters, P. W. C. Groen, M. C. M. van de Sanden, and W. A. Bongers (2019), Characterization of CO_2 microwave plasma based on the phenomenon of skin-depth-limited contraction, *Plasma Sources Sci. Technol.*, *28*(115022).

Wolf, A. J., F. J. J. Peeters, P. W. C. Groen, W. A. Bongers, and M. C. M. van de Sanden (2020a), CO_2 conversion in nonuniform discharges: Disentangling dissociation and recombination mechanisms, *J. Phys. Chem. C*, *124*, 16,806–16,819.

Wolf, A. J., T. W. H. Righart, F. J. J. Peeters, W. A. Bongers, and M. C. M. van de Sanden (2020b), Implications of thermo-chemical instability on the contracted modes in CO_2 microwave plasmas, *Plasma Sources Sci. Technol.*, *29*(025005).

Yimer, I., I. Campbell, and L. Y. Jiang (2002), Estimation of the turbulent Schmidt number from experimental profiles of axial velocity and concentration for high-Reynolds-number jet flows, *Can. Aeronaut. Space J.*, *48*, 195–200.

Zhong, H., M. N. Shneider, M. S. Mokrov, and Y. Ju (2019), Thermal-chemical instability of weakly ionized plasma in a reactive flow, *J. Phys. D: Appl. Phys.*, *52*(484001).